J. Mech. Phys. Solids 208 (2026) 106488

Contents lists available at ScienceDirect

Journal of the Mechanics and Physics of Solids

journal homepage: www.elsevier.com/locate/jmps

# Inverse elastica: A theoretical framework for inverse design of morphing slender structures

JiaHao Li [a,1], Weicheng Huang [b,1], YinBo Zhu [a], Luxia Yu [a], Xiaohao Sun [a,*], Mingchao Liu [c,*], HengAn Wu [a,*]

[a] CAS Key Laboratory of Mechanical Behavior and Design of Materials, Department of Modern Mechanics, University of Science and Technology of China city, 230027, China
[b] School of Engineering, Newcastle University, Newcastle upon Tyne, NE1 7RU, UK
[c] Department of Mechanical Engineering, University of Birmingham, Birmingham, B15 2TT, UK

ARTICLE INFO

*Keywords:*
Morphing slender structures
Inverse design
Elastica
Inverse elastica

ABSTRACT

Inverse design of morphing slender structures with programmable curvature has significant applications in various engineering fields. Most existing studies formulate it as an optimization problem, which requires repeatedly solving the forward equations to identify optimal designs. Such methods, however, are computationally intensive and often susceptible to local minima issues. In contrast, solving the inverse problem theoretically, which can bypass the need for extensive forward simulations, is highly efficient yet remains challenging, particularly for cases involving arbitrary boundary conditions, such as clamped-free and clamped-clamped boundary conditions. Here, we develop a systematic theoretical framework based on Kirchhoff rod model, termed inverse elastica, for the direct determination of the undeformed configuration from a target deformed shape along with prescribed BCs. Building upon the classical Kirchhoff rod model, inverse elastica is derived by supplementing the geometric equations of undeformed configurations. Compared to forward solving of Kirchhoff rod model, inverse elastica shows several features: reduced nonlinearity, inverse loading and solution multiplicity. Building upon inverse elastica, we develop a theory-assisted optimization strategy for cases in which the constrains of the undeformed configurations cannot be directly formulated as boundary conditions. Using this strategy, we achieve rational inverse design of complex spatial curves and curve-discretized surfaces with varying Gaussian curvatures. Our theoretical predictions are validated through both discrete elastic rod simulations and experiments. While grounded in theory, the engineering value of inverse elastica is demonstrated through design of a deployable and conformable hemispherical helical antenna. This work thus provides a novel strategy for inverse design of morphing slender structures, opening new avenues for applications in morphing structures, soft robotics, deployable radio-frequency systems, architectural design, and beyond.

## 1. Introduction

Morphing structures that adapt their shape in response to external stimuli have gained importance due to applications in flexible electronics (Xu et al., 2015; Fan et al., 2020; Liu et al., 2020), aerospace (Benvenuto et al., 2015; Huang et al., 2023), biomedical

* Corresponding authors.
*E-mail addresses:* lijh0417@mail.ustc.edu.cn (J. Li), weicheng.huang@ncl.ac.uk (W. Huang), zhuyinbo@mail.ustc.edu.cn (Y. Zhu), luxiayu@ustc.edu.cn (L. Yu), sunxiaohao@ustc.edu.cn (X. Sun), m.liu.2@bham.ac.uk (M. Liu), wuha@ustc.edu.cn (H. Wu).
[1] JL and WH contributed equally to this work.

https://doi.org/10.1016/j.jmps.2025.106488
Received 26 August 2025; Received in revised form 17 December 2025; Accepted 18 December 2025
Available online 20 December 2025

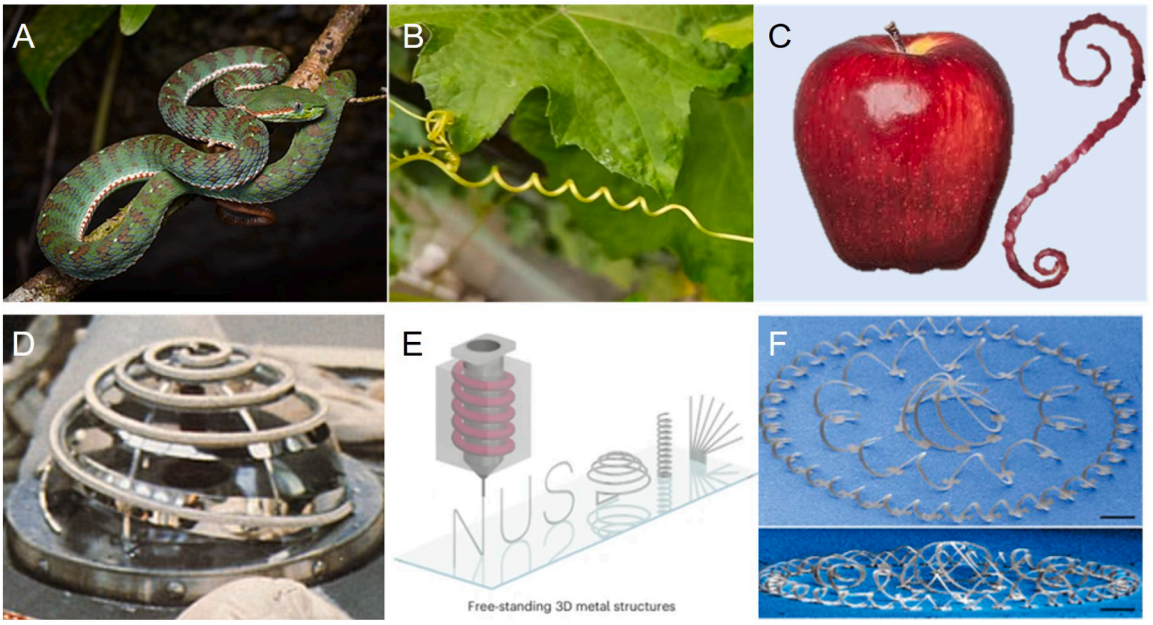


**Fig. 1.** Morphological diversity of slender structures in nature and corresponding engineering applications. (A) Arboreal adaptation demonstrated by a Trimeresurus sabahi coiling around a tree branch (Rushen, 2019). (B) A plant tendril with helix morphology under gravity. (C) A continuous helical apple peel is generated during paring. (D) The conformable hemispherical helix antenna in Venera-7. (E) Freestanding three-dimensional metal slender structures fabricated via advanced additive manufacturing technology (Ling et al., 2024). (F) Flexible electronic self-assembly through buckling of slender structures (Xu et al., 2015).

devices (Kim et al., 2019; Tong et al., 2025), and soft robotics (Shin et al., 2018; Tong et al., 2025). These systems typically use low-dimensional geometries embedded in three-dimensional (3D) space, such as two-dimensional (2D) plates/shells and one-dimensional (1D) beams/ribbons. In the past two decades, significant research has focused on 2D morphing structures. For example, Efrati et al. (2009) developed the non-Euclidean plate theory to model bilayer plate deformations, and further applied to capture helicoid-to-helix transitions in chiral seed pods (Armon et al., 2011). It further shows that this bilayer can be approximated by a monolayer model (Van Rees et al., 2017). Building on these theories, inverse design has been demonstrated using inflatable plates (Siéfert et al., 2019), 4D printing (Sydney Gladman et al., 2016), and liquid crystal elastomers (Aharoni et al., 2018; Boley et al., 2019). Machine learning has also emerged as a powerful tool for the inverse design of 2D structures. It has been applied to the inverse design of 4D-printed bilayer plates (Sun et al., 2022b, 2024). Moreover, machine learning has also been employed to design multiple morphing beams that approximate a curved surface (Cheng et al., 2023; Shen et al., 2024). However, the design of 2D morphing structures is limited by Gauss's Theorema Egregium, which states that Gaussian curvature depends solely on the surface metric (Siéfert et al., 2019). Thus, achieving large-curvature target shapes from flat plates requires significant in-plane stretching, often beyond what material expansion can provide, restricting achievable morphologies.

To address this challenge, a promising approach is to reduce the structural dimensionality. Compared with 2D morphing structures, 1D morphing structures, often called morphing slender structures, offer greater geometric flexibility, which significantly expands the design space for inverse design. In nature, slender structures such as the Trimeresurus sabahi snake (Rushen, 2019) and plant tendrils show evolutionary advantages due to their ability to adaptively change shape, enabling reliable attachment to branches and other surfaces, as illustrated in Figs. 1(A) and (B). Furthermore, ribbons represent an intermediate form between 1D and 2D structures. They combine the geometric flexibility of slender structures with the ability to discretize curved surfaces, effectively bypassing the constraints imposed by Gauss's Theorema Egregium (Li et al., 2025b). This principle is exemplified by the continuous helical peel of an apple, shown in Fig. 1(C). The geometric flexibility of slender structures holds profound significance not only in the evolutionary adaptations of organisms but also in a wide range of engineering applications. Notably, the folded hemispherical helix plays a critical role in the design of compact antennas, with its quality factor approaching the fundamental Chu-Harrington limit (Chu, 1948; Kong et al., 2016). An exemplary application is the antenna used in the Venera-7 mission, as illustrated in Fig. 1(D). Building on this, substantial advancements have been achieved in 3D printing technologies, enabling the fabrication of complex slender structures without the need for support materials, as demonstrated in Fig. 1(E) (Ling et al., 2024). In addition to these advanced printing techniques, the morphology of slender structures formed through elastic deformation represents a relatively simple yet effective strategy, which is a widely applied strategy in flexible electronic fabrication as illustrated in Fig. 1(F) (Xu et al., 2015; Fan et al., 2020; Cheng et al., 2023).

Morphing slender structures can be broadly classified into two categories based on their fundamental actuation mechanisms. The first category comprises structures actuated by external physical stimuli such as temperature gradients (Timoshenko, 1925), hydration

(Armon et al., 2011; Chen et al., 2011; Shin et al., 2018; Li et al., 2025b), or pH variations (Sawa et al., 2011). These materials often employ bilayer architectures, where strain mismatch between dissimilar layers induces bending and twisting deformations (Armon et al., 2011; Chen et al., 2011; Li et al., 2025b,c). Over the past century, the inverse design of such bilayer systems has been extensively explored, progressing from simple beam models to uniform deformations in helical ribbons (Timoshenko, 1925; Armon et al., 2011; Chen et al., 2011), and more recently culminating in a comprehensive theoretical framework for complex spatial curves with various curvature and torsion (Li et al., 2025b). Despite the maturity of the design theory for morphing bilayer ribbons, experimental fabrication remains challenging, particularly in precisely encoding parameters such as the volume fraction of swelling component and the fibril orientation angle within the material. The second category consists of morphing slender structures that are more readily fabricated experimentally by regulating elastic deformation. Designing the deformed configuration (DC) typically involves tuning the stiffness distribution or intrinsic curvatures of the undeformed configuration (UC) as primary design parameters. Manipulating stiffness distribution is a common approach in soft electronics; however, it is limited by a restricted design space and often requires complex boundary loading conditions to achieve effective morphing (Fan et al., 2020; Liu et al., 2020; Zhang et al., 2022; Kansara et al., 2023). For example, previous studies have discretized rotating bodies with varying Gaussian curvatures into multiple radially arranged beams with tailored width profiles. Morphing toward the target shape is realized by precisely controlling the Euler buckling of each beam, which necessitates simultaneous regulation of boundary displacements across all beams (Fan et al., 2020; Liu et al., 2020; Yang et al., 2023). To overcome the challenges posed by such complex loading requirements, a more robust and comprehensive theoretical framework for inverse design of morphing slender structures is essential.

Regulating the intrinsic curvature of the UC enables a more straightforward inverse design process, as it typically requires only simple boundary conditions (BCs). Prior studies have drawn inspiration from natural deformation processes, such as the bending of curling hair or tendrils with intrinsic growth curvature under gravity, where one end of the rod is clamped and the other remains free. As a result, clamped-free BCs are commonly adopted in inverse design theories. Bertails-Descoubes et al. investigated the inverse design of suspended Kirchhoff rods under gravity, both theoretically and numerically (Derouet-Jourdan et al., 2010, 2013; Bertails-Descoubes et al., 2018). They demonstrated that a unique inverse solution exists under clamped-free BCs. Subsequent works by Qin et al. (2022) and Tong et al. (2025) explored the two-dimensional cases. Although inverse design under gravity-driven clamped-free conditions has been studied, its applicability remains restricted to a narrow class of materials. This limitation arises because the gravity-elastic parameter must lie within a narrow range for the solution to be physically realizable (Bertails-Descoubes et al., 2018; Qin et al., 2022; Tong et al., 2025). Moreover, most existing studies formulate inverse design as an optimization problem, in which the discrepancy between forward-computed and target configurations is minimized (Derouet-Jourdan et al., 2010, 2013; Qin et al., 2020). However, such optimization-based approaches often incur excessive computational costs, because the underlying physical mechanism of inverse design remains unclear. This motivates a broader challenge: how to establish a general inverse theory that transcends the limitations of gravity and enables the inverse design of morphing slender structures under arbitrary BCs? At its core, this question reflects a fundamental inversion of the classical elastica problem. The Kirchhoff rod equations, as formulated in classical elastica theory (Love, 1944; Audoly and Pomeau, 2000; O'Reilly, 2017), are used to determine the DC from a known UC. In contrast, inverse design based on intrinsic curvature aims to reconstruct the UC from a desired DC. Addressing this challenge necessitates the development of a general inverse elastica theory.

In this work, we build an inverse design theory, termed the 'inverse elastica', based on the classical Kirchhoff-Clebsch rod theory (Love, 1944; Audoly and Pomeau, 2000; O'Reilly, 2017). As a unified theoretical framework, the inverse elastica enable the direct determination of the UC from the DC under arbitrary BCs and external loads. We begin with a brief review of the forward problem in Section 2.1, followed by the formulation and theoretical development of the inverse problem in Section 2.2. Then we show the characters of inverse elastica by comparing with the forward solving of Kirchhoff model in Section 2.3. Because certain constraints on the UC morphology, such as minimum curvature or minimum volume occupancy, are not easily expressed as explicit BCs, we develop a theory-assisted optimization strategy for inverse design in Section 3.1. Section 3.2 extends the framework to the inverse design of complex spatial curves, such as the trefoil knot, and helix discretized curved surfaces with varying Gaussian curvatures, including the torus, cone, sphere, and hyperboloid. Furthermore, in Section 3.3 we demonstrate the potential engineering application of the framework through the inverse design of a deployable and conformable hemispherical antenna. Finally, Section 4 discusses the main features of the inverse elastica theory and outlines potential directions for future research. Conclusions are summarized in Section 5.

## 2. The theoretical framework for inverse design

In this section, we present the forward and inverse frameworks for morphing slender structures based on elastica theory. We begin by briefly reviewing the classical forward Kirchhoff model, then develop the corresponding inverse elastica theory. Finally we conclude with a comparative discussion of the two models.

### 2.1. Forward elastica problem

Governing equations The forward problem is defined as determining the DC of slender structures based on a known UC, material properties, applied boundary displacements, and loading conditions. We use the classical Kirchhoff model to describe the mechanics of a slender rod and ribbon. The Kirchhoff model, which accounts for bending and twisting while neglecting stretching, shearing, and cross-sectional deformation, has been widely used to predict the deformation behavior of slender structures under specified BCs (Audoly and Pomeau, 2000; O'Reilly, 2017). The Kirchhoff theory can serve as a solution to the forward problem. As shown in Fig. 2, the DC is denoted as $\mathbf{\Gamma}(s)$, and the UC is denoted as $\mathbf{\Gamma}_0(s)$, where $s \in [0, L]$ is the arc length parameter, and $L$ is the total length of the

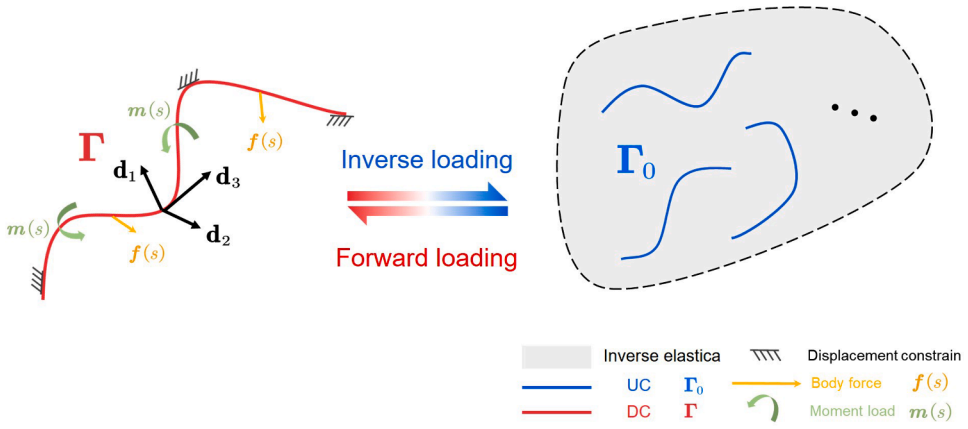


**Fig. 2.** Inverse elastica and elastica under arbitrary displacement boundary conditions and external loading. The red curve represents the DC, with the tangent vector $\mathbf{d}_3$ and the two material vectors $\mathbf{d}_1$ and $\mathbf{d}_2$ shown as black arrows, while the blue curve denotes the UC. A specific DC corresponds to a family of UC determined by the applied body forces, moment loads, and displacement constraints.

slender system. We use a subscript with zero $(\cdot)_0$ for the evaluation on the UC. Based on the force balance and the moment balance, the equilibrium equation is given by

$$\mathbf{F}'(s) + \mathbf{f}(s) = \mathbf{0}, \tag{1}$$

$$\mathbf{M}'(s) + \mathbf{d}_3(s) \times \mathbf{F}(s) + \mathbf{m}(s) = \mathbf{0}, \tag{2}$$

where $\mathbf{f}(s)$ and $\mathbf{m}(s)$ are the external force and moment density loads, $\mathbf{F}(s)$, $\mathbf{M}(s)$ are the internal force and internal moment of the slender system, $(\cdot)' = \partial(\cdot)/\partial s$ is the derivative of variable $(\cdot)$ to arc length parameter $s$, and $\mathbf{d}_3(s)$ is the tangent of the rod. Later, we ignore the arc length parameter $(s)$ for simplification.

Note that we use linear elastic constitutive model in Kirchhoff model, thus the moment can be expressed as the difference between the material curvature of DC and UC. We can read:

$$\bar{\mathbf{M}} = (\boldsymbol{\omega} - \boldsymbol{\omega}_0)\mathbf{S}, \tag{3}$$

where $\boldsymbol{\Omega} = \mathrm{skew}(\boldsymbol{\omega})$ is the rotation tensor, $\boldsymbol{\omega} = \{\omega_1, \omega_2, \omega_3\}$ is the Darboux vector in the DC, $\boldsymbol{\omega}_0$ is the Darboux vector in the UC, $\mathbf{S} = \mathrm{diag}(\{\mathrm{EI}_1, \mathrm{EI}_2, \mathrm{GJ}\})$ is the stiffness matrix. And the physical vectors for the moment are transformed into the component vector $\bar{\mathbf{M}} = \{M_1, M_2, M_3\}$ (and $\mathbf{M} = \bar{\mathbf{M}}\mathbf{D}$).

To solve Eq. (1) and (2), we expand the other physical vectors in the local deformed material frame (DC), $\mathbf{D} = \{\mathbf{d}_1, \mathbf{d}_2, \mathbf{d}_3\}^T$, (where $\mathbf{d}_1$ and $\mathbf{d}_2$ are the two material directors), the equilibrium equation and the linear constitutive equation are given as

$$\bar{\mathbf{F}}' + \bar{\mathbf{F}}\boldsymbol{\Omega} + \bar{\mathbf{f}} = 0, \tag{4}$$

$$\bar{\mathbf{M}}' + \bar{\mathbf{M}}\boldsymbol{\Omega} + \bar{\mathbf{F}}\boldsymbol{\Lambda} + \bar{\mathbf{m}} = 0, \tag{5}$$

$$\boldsymbol{\Lambda} = \begin{pmatrix} 0 & 1 & 0 \\ -1 & 0 & 0 \\ 0 & 0 & 0 \end{pmatrix}, \tag{6}$$

Also, the physical vectors for the force are transformed into the component vector, i.e., $\bar{\mathbf{F}} = \{F_1, F_2, F_3\}$ is the component vector of internal force vector $\mathbf{F}$ in material frame thus $\mathbf{F} = \bar{\mathbf{F}}\mathbf{D}$, and, similar for $\bar{\mathbf{f}} = \{f_1, f_2, f_3\}$ (and $\mathbf{f} = \bar{\mathbf{f}}\mathbf{D}$), and $\bar{\mathbf{m}} = \{m_1, m_2, m_3\}$ (and $\mathbf{m} = \bar{\mathbf{m}}\mathbf{D}$).

Boundary conditions The rotation in 3D space can be described with the quaternion (Sun et al., 2022a), thus we supply the geometry equations to include the displacement BCs

$$\boldsymbol{\Gamma}' = \boldsymbol{R}_3^T, \tag{7}$$

$$\boldsymbol{q}' = \mathbf{Q}\boldsymbol{q}, \tag{8}$$

where, $\boldsymbol{\Gamma} = \{x,\ y,\ z\}^T$ is the DC, $\boldsymbol{q} = \{q_0, q_1, q_2, q_3\}^T$ is the quaternion vectors, $\boldsymbol{R}_3$ is the third row of rotation matrix $\boldsymbol{R}$ and $\mathbf{Q}$ is a matrix,

$$\boldsymbol{R} = 2\begin{pmatrix} q_0^2 + q_1^2 - 1/2 & q_1q_2 + q_0q_3 & q_1q_3 - q_0q_2 \\ q_1q_2 - q_0q_3 & q_0^2 + q_2^2 - 1/2 & q_2q_3 + q_0q_1 \\ q_1q_3 + q_0q_2 & q_2q_3 - q_0q_1 & q_0^2 + q_3^2 - 1/2 \end{pmatrix}, \tag{9}$$

and

$$\mathbf{Q} = \begin{pmatrix} 0 & -\boldsymbol{\omega} \\ \boldsymbol{\omega}^T & \boldsymbol{\Omega} \end{pmatrix}. \tag{10}$$

Combine Eqs. (4) ~ (8), we can solve the forward problem as a boundary value problem (BVP) under the given displacement BCs of boundary displacement $\boldsymbol{\Gamma}(0)$, $\boldsymbol{\Gamma}(L)$ and rotation angle $\boldsymbol{q}(0)$, $\boldsymbol{q}(L)$, where $L$ is the length of the rod.

In this section, we have briefly reviewed the Kirchhoff model as a solution for forward problem of slender structures. In the next section, we will build inverse elastica theory.

### 2.2. Inverse elastica theory

The inverse problem is defined as determining the UC with the given DC, material properties, applied loading and boundary displacement. Note that for the inverse process solving UC from DC, the solution is also required to meet the force and moment balance in DC. Therefore, the physical equation of inverse elastica theory can be read from the Kirchhoff equation directly:

$$\begin{cases} \bar{\mathbf{F}}' + \bar{\mathbf{F}}\boldsymbol{\Omega} + \bar{\mathbf{f}} = \mathbf{0} \\ \bar{\mathbf{M}}' + \bar{\mathbf{M}}\boldsymbol{\Omega} + \bar{\mathbf{F}}\boldsymbol{\Lambda} + \boldsymbol{m} = \mathbf{0} \\ \bar{\mathbf{M}} = (\boldsymbol{\omega} - \boldsymbol{\omega}_0)\mathbf{S} \end{cases}, \tag{11}$$

Our objective is to control the displacements at both ends of the rod (i.e., at $s = L$ and $s = 0$). Consequently, the inverse formulation necessitates an additional geometric constraint equation for UC. To this end, we introduce the requisite geometric constraint:

$$\boldsymbol{\Gamma}_0' = \boldsymbol{R}_{03}^T, \tag{12}$$

$$\boldsymbol{q}_0' = \mathbf{Q}_0 \boldsymbol{q}_0. \tag{13}$$

Where $\boldsymbol{\Gamma}_0 = \{x_0(s), y_0(s), z_0(s)\}^T$ is coordination of center line of UC as a function of arc length parameter $s$, $\boldsymbol{q}_0 = \{q_{00}(s), q_{01}(s), q_{02}(s), q_{03}(s)\}^T$ is the quaternion vector of UC, $\boldsymbol{R}_{03}$ is the third row of rotation matrix $\boldsymbol{R}_0$ and $\mathbf{Q}_0$ is a quaternion matrix for UC. $\boldsymbol{R}_0$ and $\mathbf{Q}_0$ can be written as

$$\boldsymbol{R}_0 = 2\begin{pmatrix} q_{00}^2 + q_{01}^2 - 1/2 & q_{01}q_{02} + q_{00}q_{03} & q_{01}q_{03} - q_{00}q_{02} \\ q_{01}q_{02} - q_{00}q_{03} & q_{00}^2 + q_{02}^2 - 1/2 & q_{02}q_{03} + q_{00}q_{01} \\ q_{01}q_{03} + q_{00}q_{02} & q_{02}q_{03} - q_{00}q_{01} & q_{00}^2 + q_{03}^2 - 1/2 \end{pmatrix}, \tag{14}$$

and

$$\mathbf{Q}_0 = \begin{pmatrix} 0 & -\boldsymbol{\omega}_0 \\ \boldsymbol{\omega}_0^T & \boldsymbol{\Omega}_0 \end{pmatrix}. \tag{15}$$

Finally we obtain the complete inverse elastica theory for morphing slender structures

$$\begin{cases} \bar{\mathbf{F}}' + \bar{\mathbf{F}}\boldsymbol{\Omega} + \bar{\mathbf{f}} = \mathbf{0} \\ \bar{\mathbf{M}}' + \bar{\mathbf{M}}\boldsymbol{\Omega} + \bar{\mathbf{F}}\boldsymbol{\Lambda} + \bar{\mathbf{m}} = \mathbf{0} \\ \bar{\mathbf{M}} = (\boldsymbol{\omega} - \boldsymbol{\omega}_0)\mathbf{S} \\ (\boldsymbol{\Gamma}_0)' = \boldsymbol{R}_{03}^T \\ (\boldsymbol{q}_0)' = \mathbf{Q}_0 \boldsymbol{q}_0 \end{cases}, \tag{16}$$

Note that only inverse design of morphing slender structure under clamped-free BCs can be solved uniquely in theory in previous works (Miller et al., 2014; Bertails-Descoubes et al., 2018). However, with inverse elastica, we can achieve the inverse design of slender structure under general BCs (e.g. clamped-clamped BCs). Specifically, by using displacement BCs to solve Eq. (16) we can obtain the UC from the target DC directly.

In this section, the inverse elastica theory is established by supplying the geometric equation of the UC. For a deeper understanding, a brief comparison with the forward Kirchhoff trod model is elaborated in Section 2.3.

### 2.3. Comparison with forward solving of Kirchhoff model

The Kirchhoff rod model is widely used to describe the elastic deformation of slender structures based on the Kirchhoff-Love assumption. Before introducing the main characteristics of inverse elastica, it is necessary to clarify that the proposed theory does not constitute a new rod model. Instead, it represents a theoretical framework for inverse design built upon the classical Kirchhoff rod theory, because the same Kirchhoff-Love assumption regarding cross-sectional behavior is adopted in inverse elastica. Nevertheless, despite sharing the same underlying mechanical assumptions, inverse elastica differs from the conventional forward solution of the Kirchhoff rod model in terms of problem formulation and the choice of unknowns.

Firstly, note that in Eq. (16) the unknown is $\boldsymbol{\omega}_0$ rather than $\boldsymbol{\omega}$ for inverse problem. Therefore the nonlinearity of inverse elastica is reduced because $\boldsymbol{\Omega}$ as a known is no longer coupled with $\bar{\mathbf{M}}$ and $\bar{\mathbf{F}}$. Secondly, for the inverse problem, we can solve $\bar{\mathbf{F}}$, $\bar{\mathbf{M}}$, $\boldsymbol{\Gamma}_0$

and $\boldsymbol{q}_0$ from Eq. (16) with the given displacement BCs $\boldsymbol{q}_0(0)$, $\boldsymbol{q}_0(L)$ and $\boldsymbol{\Gamma}_0(0)$, $\boldsymbol{\Gamma}_0(L)$ for UC. This is similar to the forward loading but different, thus we define it as inverse loading. Futhermore, as discussed in previous study, although it has been realized the solution to clamped-clamped BCs is not unique (Bertails-Descoubes et al., 2018), a general theory to achieve the inverse design is still challenging. Suppose that we give a random initial value of $\bar{\mathbf{F}}(L)$ and $\bar{\mathbf{M}}(L)$, the solution $\boldsymbol{\omega}_0$ is a certain UC. This means that, under displacement BCs (e.g., clamped-clamped), there exists a family of UC corresponding to a single DC, as illustrated in Fig. 2. This is because a clamped boundary can support arbitrary magnitudes of force and moment. For the case of multiple displacement BCs as in a multi-point boundary value problem, the system can be simplified to a set of coupled BVPs, as shown in previous studies (Yu et al., 2023).

There are two approaches to achieve inverse design: one is obtaining UC by solving Eq. (16) directly. Using this approach we show the analytical solution for inverse design of planar curve in Appendix A and use numerical continuation to design a helix inversely through inverse loading in Appendix B. The other is using the theory-assisted optimization method. In certain circumstances, we want the UC to exhibit certain characteristics that are difficult to be expressed as explicit BCs. For example, we want to minimize the height variance of the helix discretized surfaces to reduce the volume. Under this situation, solving the inverse elastica equation as a BVP is generally not an effective approach for inverse design. To address this challenge, we present a theory-assisted optimization strategy and show some inverse design cases under clamped-clamped BCs in next section.

## 3. Inverse design enabled by theory-assisted optimization

In Section 2, we have developed a general inverse design theory and understood the three characteristics underlaying the inverse elastica theory by solving the inverse equation as BVP analytically and numerically. In fact, under some situations our goal is to select the UC with certain characteristics. However, the certain characteristics that we want for the UC are not easy to be expressed as the displacement BCs for Eq. (16). For example, if we want UC to be as close as possible to a straight line, which means the curvature of UC should be as small as possible, the problem can be summarized as finding the initial value to minimize the curvature: $\min_{\{\boldsymbol{F}(0),\boldsymbol{M}(0)\}} \int_0^L \omega_{10}^2 + \omega_{20}^2 ds$, where $\omega_{10}$ and $\omega_{20}$ are the material curve of UC in width and thickness directions. This is an optimization problem and it is not easy to be expressed as BCs for Eq. (16). Recall that we have demonstrate the multiplicity of solutions of inverse elastica, which means that for clamped-clamped BCs when we select arbitrary values of $\bar{\mathbf{F}}(0), \bar{\mathbf{M}}(0)$, we can always obtain the UC by solving Eq. (16) as an initial value problem (IVP). Therefore, we propose a theory-assisted optimization method to achieve some complex inverse design cases under clamped-clamped BCs.

### 3.1. Theory-assisted optimization

As shown in Fig. 3, we first define the inverse design as an optimization problem:

$$\begin{aligned} \left\{\bar{\mathbf{F}}^*(0), \bar{\mathbf{M}}^*(0)\right\} &= \min_{\{\boldsymbol{F}(0),\boldsymbol{M}(0)\}} f\left(\boldsymbol{\omega}_0, \boldsymbol{\Gamma}_0\right), \\ & s.t. \mathcal{I}nv\mathcal{E}elastica\left(\boldsymbol{\omega}_0\right) = \mathbf{0}, \end{aligned} \tag{17}$$

where $\left\{\bar{\mathbf{F}}^*(0), \bar{\mathbf{M}}^*(0)\right\} \in \mathcal{R}^{6\times 1}$ is the optimal initial value of force and moment, $\mathcal{I}nv\mathcal{E}lastica\left(\boldsymbol{\omega}_0\right)$ describes the underlying physics constraints from the inverse elastica theory in Eq. (16), and $f(\boldsymbol{\omega}_0, \boldsymbol{\Gamma}_0)$ is the loss function, which represents the certain characteristics we want UC to possess. Here we combine inverse elastica theory and Nelder-Meaed method (Singer and Nelder, 2009) to achieve the optimization. As shown in Fig. 3, firstly we give an initial guess of $\left\{\bar{\mathbf{F}}(0), \bar{\mathbf{M}}(0)\right\}$, then the material curvature $\boldsymbol{\omega}_0$ is calculated from inverse elastica theory Eq. (16). Using the geometry equation, the coordination of UC $\boldsymbol{\Gamma}_0$ can be calculated from the material curvature $\boldsymbol{\omega}_0$. Finally $\{\boldsymbol{\omega}_0, f(\boldsymbol{\omega_0}, \boldsymbol{\Gamma}_0)\}$ is obtained as the input for Nelder-Mead method. The Nelder-Mead algorithm is a direct search method that optimizes the loss function f(x) without requiring gradient information. Starting from an initial simplex of 7 points $\boldsymbol{\omega}_0^i (i = 1 \dots 7)$ in six-dimensional space, it iteratively updates the simplex through reflection, expansion, contraction, and shrink operations based on the function values $f(\boldsymbol{\omega}_0^i, \boldsymbol{\Gamma}_0)$ at each vertex. The algorithm replaces the worst vertex with a better point in each iteration, gradually moving the simplex toward the minimum region. The process continues until the simplex size falls below a specified tolerance or the improvement in function value becomes negligible, providing an approximate solution to minimize $f(\boldsymbol{\omega_0}, \boldsymbol{\Gamma}_0)$. Note that the theory-assisted optimization method is much more efficient than forward optimization. And we use the inverse design of a cardioid for comparison in Appendix C. Some more complicated inverse design demonstrations under clamped-clamped BCs are presented with the proposed theory-assisted optimization strategy in Section 3.2. We declare that for all of the cases, the physical parameters are parameterized by arc-length $s$ and $s$ is a function of parameter $t$, while the left end refers to the end at $s = 0$ and right end refers to $s = L$.

### 3.2. Inverse design demonstration

#### 3.2.1. The trefoil knot

In previous study, Moulton et al. (2018) demonstrated that a ribbon can deform to a stable open knot, but a rod with circular cross section cannot. Inspired from this work, we try to find a ribbon as UC with the smallest possible curvature to deform into a close trefoil knot. The close trefoil knot means that a ribbon whose middle line is along with the standard trefoil knots in Eq. (18) and the direction of the normal vector is continuous; hence the twisting angle between the reference frame and material frame is set

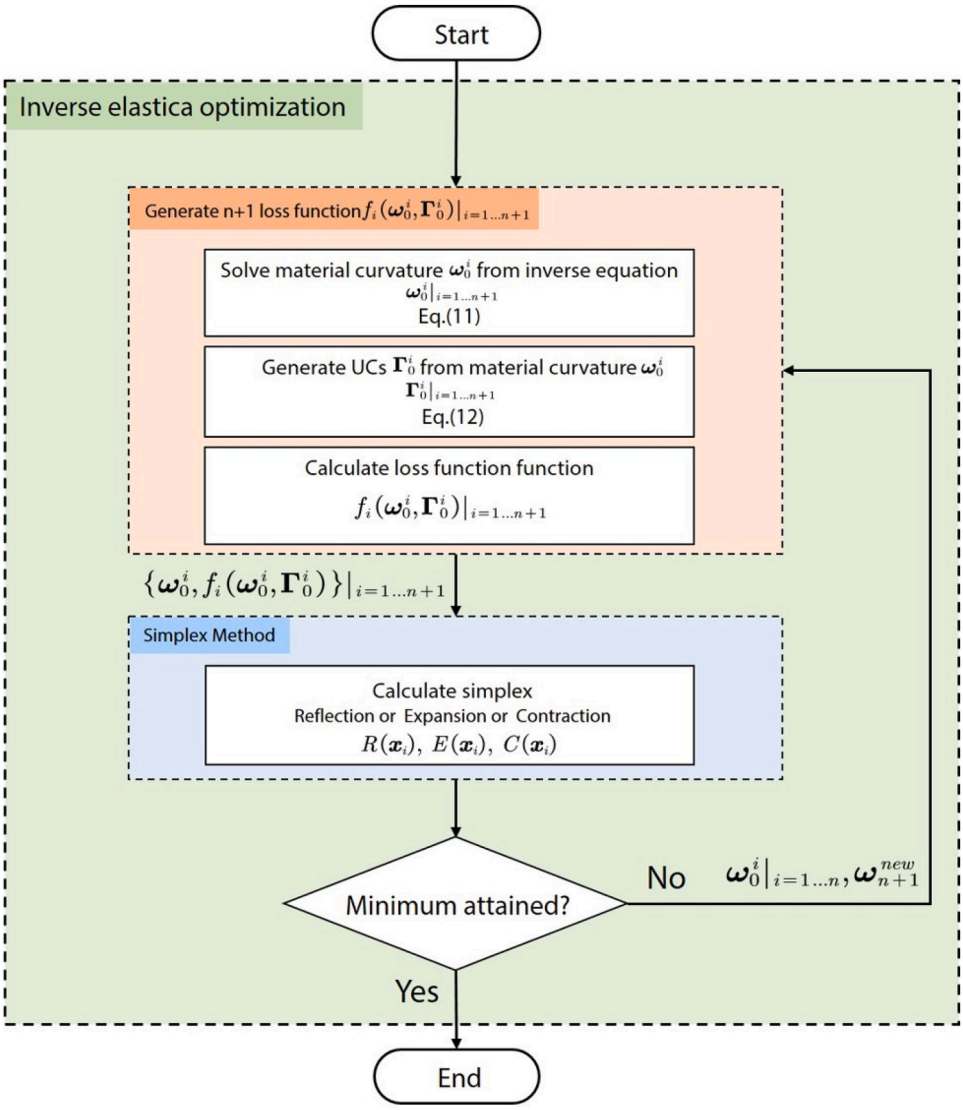


**Fig. 3.** The algorithm flow chart of theory-assisted optimization.

as $(\pi - 0.9192) * t$ to ensure the direction of normal vectors at the two ends are the same as shown in Fig. 4(A).

$$\begin{cases} x(t) = \sin(2\pi t) + 2\sin(4\pi t) \\ y(t) = \cos(2\pi t) - 2\cos(4\pi t) \\ z(t) = -\sin(6\pi t) \end{cases} \quad t \in [0, 1.0). \tag{18}$$

The loss function is defined as:

$$f(\boldsymbol{\omega}_0, \boldsymbol{\Gamma}_0) = \min_{\{\boldsymbol{F}(0), \boldsymbol{M}(0)\}} \frac{N}{L} \int_0^L (\omega_{10}^2 + \omega_{20}^2) ds, \tag{19}$$

where $N$ is the number of the discrete point. By minimizing Eq. (19), the optimized UC is obtained, as shown in Fig. 4(A). The evolution of the loss function during the optimization process is illustrated in Fig. 4(B). Notably, a sharp decrease from approximately 2100 to 1300 around the 10th iteration suggests a sudden transition between two quasi-steady states. The curvature and torsion profiles of the DC and the UC are presented in Figs. 4(C) and (D), respectively. It is observed that the optimized UC maintains geometric symmetry with respect to the midpoint, i.e., at $s/L = 0.5$. To verify our theory, DER simulation is performed and the results are shown with the green points in Figs. 4(C) and (D). The simulation results are consistent with our theoretical solution and the forward loading video is shown in Appendix F.

In this section, we find the UC with minimal curvature by our inverse elastica theory for a close trefoil knot as DC. In the following section, we are more concerned about finding the UC of helix discretized curved surfaces with different Gaussian curvatures.

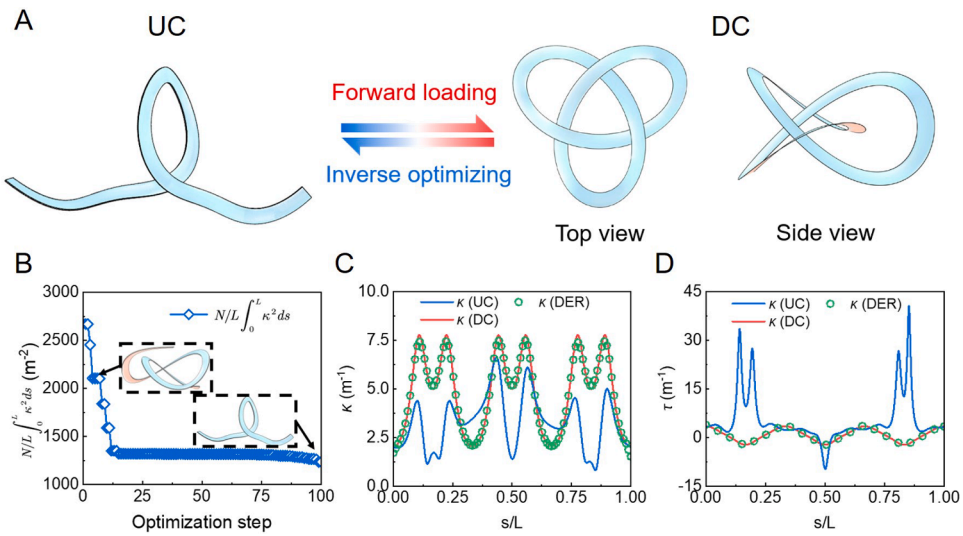


**Fig. 4.** Inverse design of a trefoil knot. (A) Elastic deformation from an open ribbon as UC to a trefoil knot as DC. (B) The value of the loss function during the optimization process. (C) The curvature of UC (blue line), DC (red line) and DER verification (green points). (D) The torsion of UC (blue line), DC (red line) and DER verification (green points).

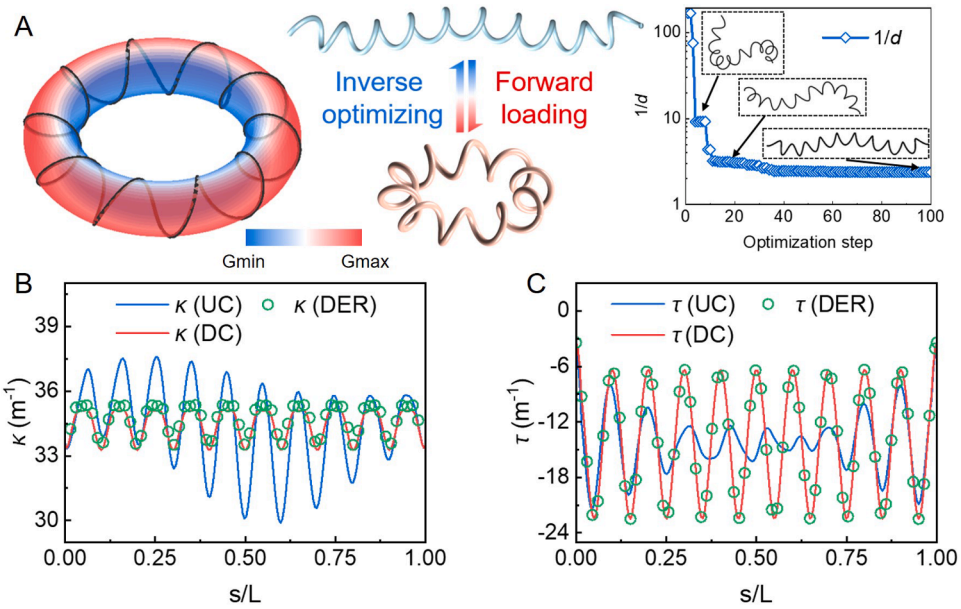


**Fig. 5.** Inverse design of a helix discretized torus. A helix discretized torus exhibiting both negative and positive Gaussian curvature, with the colormap ranging from blue (minimum Gaussian curvature) to red (maximum Gaussian curvature) (B) Elastic deformation from a spring as UC to a helix discretized torus as DC. (C) The value of the loss function during the optimization process. (D) The curvature of UC (blue line), DC (red line) and DER verification (green points). (E) The torsion of UC (blue line), DC (red line) and DER verification (green points).

### *3.2.2. The torus*

The inverse elastica theory enables the design of UC for spatial curves exhibiting complex topological features. Moreover, it facilitates the construction of UCs for specific types of DC, such as those that helix discretized curved surfaces with various Gaussian curvatures.

The torus is a geometrically rich surface characterized by regions of both positive and negative Gaussian curvature. Such configurations are frequently encountered in various biological systems in nature (Wang et al., 2023, 2025). Here we choose a helix

discretized torus as the second example as shown in Fig. 5(A). The equation of the helix discretized torus can be written as:

$$\begin{cases} x(t) = (r + R\cos(2\pi Nt))\cos(2\pi t) \\ y(t) = (r + R\cos(2\pi Nt))\sin(2\pi t) \\ z(t) = r\sin(2\pi Nt) \end{cases}, \tag{20}$$

where $R$ and $r$ are the radius of torus respectively, $N$ is a positive integer and determines the number of turns of the spiral wire on the torus. For this case, we choose $R = 4r = 0.1$, $N = 10$. Here, the UC is desired to be as slender as possible to facilitate compact storage. Accordingly, the objective function is formulated as:

$$f(\boldsymbol{\omega}_0, \boldsymbol{\Gamma}_0) = 1/d = \frac{1}{\sqrt{(x(0) - x(1))^2 + (y(0) - y(1))^2 + (z(0) - z(1))^2}}. \tag{21}$$

For the torus, its volume can be approximated by that of the circumscribed cylinder, given by $2\pi r(R + r)^2$, while the volume of the slender UC is estimated as $2\pi^2 r^2 R$. Accordingly, the volume ratio between the UC and the DC is approximated as $\frac{\pi r/R}{(1+r/R)^2}$. In this study, we set $r/R = 0.25$, resulting in a volume reduction ratio of approximately 0.5, indicating that the volume of the UC is only half that of the DC. As shown in Fig. 5(B), the optimized UC exhibits symmetry but deviates from a conventional straight helix, suggesting that a standard toroidal helix (Eq. (20)) cannot be obtained by simply clamping the ends of a straight helical spring. In Fig. 5(C), three plateau regions are observed in the optimization curve, indicating the occurrence of steady-state transitions during the optimization process, similar to those encountered in the forward problem (Yu and Hanna, 2019; Yu et al., 2021, 2023). Although a detailed bifurcation analysis of the inverse elastica equations could be performed using continuation methods (Doedel et al., 2007; Yu and Hanna, 2019), our objective here is to obtain UCs with specific geometric characteristics. Therefore, instead of analyzing the bifurcation process in detail, we adopt a direct optimization approach to obtain the desired UC. The curvature and torsion distributions of the DC and UC are shown in Figs. 5(D) and (E), respectively. The accuracy of the inverse elastica solution is further validated through forward simulation using the discrete elastic rod (DER) method, demonstrating the correctness of the proposed inverse design theoretical framework.

### 3.2.3. Curve discretized surfaces

Previously, we investigated the toroidal helix as a discretization of a curved surface exhibiting both positive and negative Gaussian curvatures simultaneously. In this section, we extend the study to three representative helix discretized curved surfaces: the cone, the sphere, and the hyperboloid, which typify surfaces with zero, positive, and negative Gaussian curvature, respectively.

For these three surfaces, the specific equations are shown in Appendix D and our goal is to minimize the height variance in order to reduce spatial volume occupancy. Accordingly, we define the loss function as the variance of the $z$-coordinate, which serves as a measure of vertical compression. This can also be interpreted as:

$$f(\boldsymbol{\omega}_0, \boldsymbol{\Gamma}_0) = \frac{1}{L}\int_0^L (z - \int_0^L z ds/L)^2 ds. \tag{22}$$

As shown in Fig. 6, the UC obtained by our theory is well consistent with the experiments and DER simulations. The details of the experiment settings is shown in Appendix D.

The optimized height variance is illustrated in Fig. 7(A). The results demonstrate that a spherical helix can be achieved by stretching a very flat UC. Notably, previous studies have required complex BCs-such as impact or multi-point compression-to morph a structure into a spherical shape (Fan et al., 2020; Lee et al., 2020; Liu et al., 2020; Kansara et al., 2023). In contrast, our approach enables the design of such UCs using inverse elastica theory, allowing the structure to transform into a helix-discretized sphere simply by clamping the two ends. As shown in Fig. 7(A), the height variance of cone is reduced from $1.2e^{-2}$ to $2.0e^{-4}$, the height variance of sphere is reduced from $2.0e^{-4}$ to $3.5e^{-6}$ and the height variance of hyperboloid is reduced from $1.8e^{-4}$ to $4.0e^{-5}$, respectively. The height variance of these three types of helix discretized surfaces are reduced by one to two orders of magnitude.

It is worth noting that the height variance of the cone and hyperboloid helices are not as small as that of the sphere. This behavior can be interpreted through the concept of inverse loading, as introduced in the Section 2.3. Inverse loading, though analogous in outcome to forward loading, arises from a fundamentally different physical mechanism. Viewing the optimization process as a form of inverse loading provides insight into the results. When a cone or hyperboloid helix is compressed under clamped-clamped BCs, the central region tends to bulge outward (as seen in Figs. 6(A) and (C)). This geometric response increases the height variance under large compression, thereby limiting the achievable height variance.

All of the cases are verified with DER simulations, the calculated error between our theory and DER verifications as shown in Fig. 7(B), the error is calculated by Eq. (23):

$$\text{Error} = \sqrt{(x_0^i - x_{DER}^i)^2 + (y_0^i - y_{DER}^i)^2 + (z_0^i - z_{DER}^i)^2}/L, \tag{23}$$

where $x_0^i, y_0^i, z_0^i$ are the discretized points of DC, $x_{DER}^i, y_{DER}^i, z_{DER}^i$ are the verified results from DER. The numerical results show that the error of our theory is controlled within 5 % as shown in Fig. 7(B).

In summary, this section demonstrates the inverse design of helix discretized curved surfaces using the inverse elastica framework. To further illustrate the practical relevance of our inverse elastica theory, an engineering application is presented in Section 3.3.

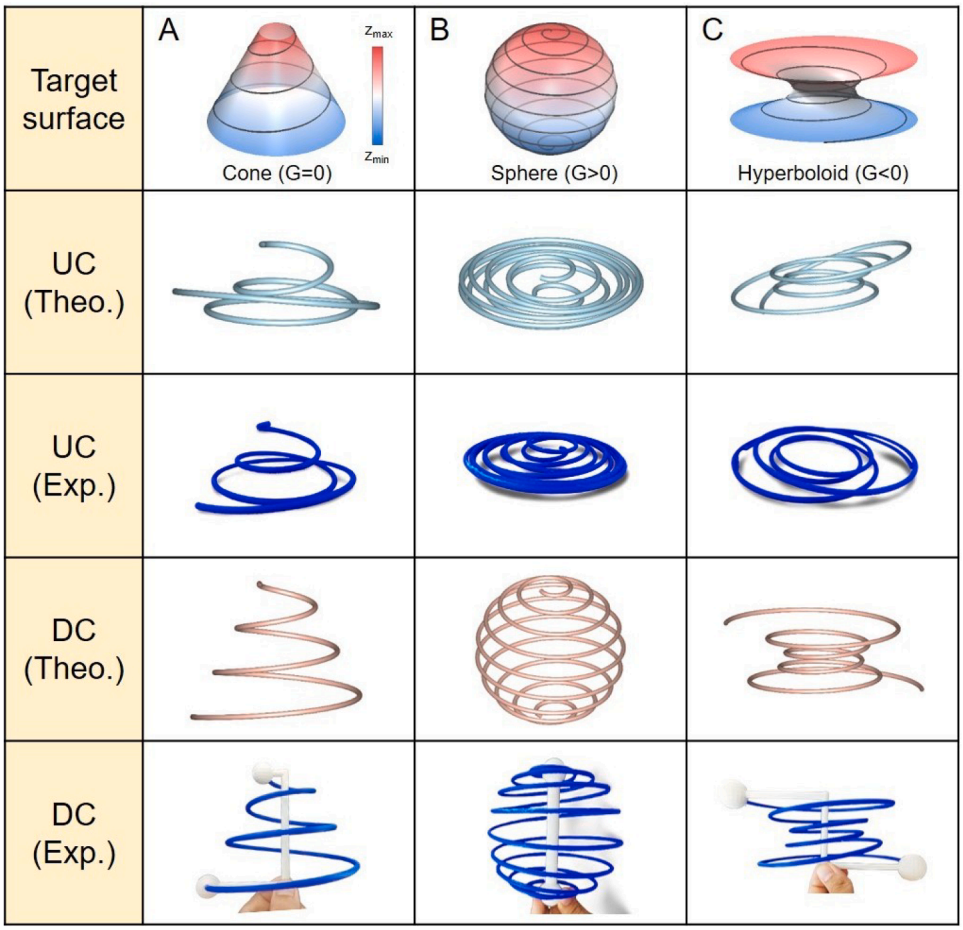


**Fig. 6.** Inverse design of three helix discretized surfaces with zero (cone), positive (sphere) and negative (hyperboloid) Gaussian curvatures. (A) Inverse design of a helix discretized cone with zero Gaussian curvature. (B) Inverse design of a helix discretized sphere with positive Gaussian curvature. (C) Inverse design of a helix discretized hyperboloid with negative Gaussian curvature.

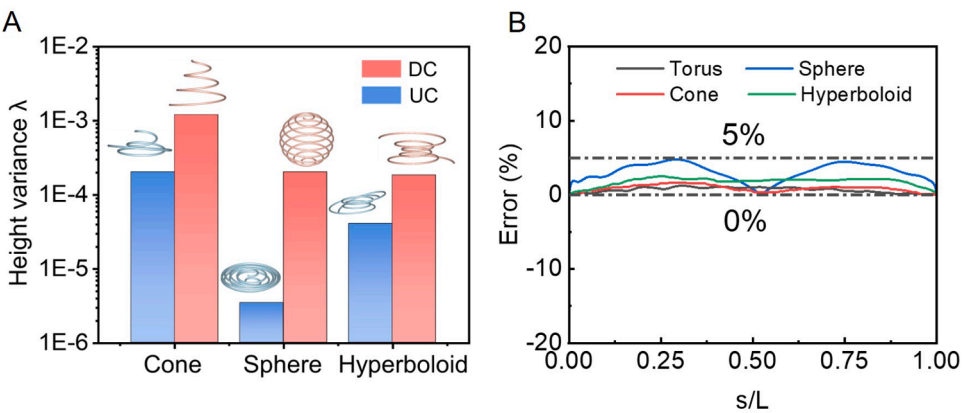


**Fig. 7.** The height variance of helix discretized surfaces with different Gaussian curvatures and the error analysis between theoretical results and DER verifications (A) Height variance of DC and UC for helix discretized cone, sphere and hyperboloid surfaces respectively. (B) The error between target shape and DER verification results for helix discretized torus, cone, sphere and hyperboloid surfaces respectively.

### 3.3. Engineering application: inverse design of a conformable hemispherical helix antenna

In Section 3.2, we demonstrated the inverse design of curved surfaces discretized using a complex helical curves. However, in certain engineering applications, it is necessary to design a ribbon that conforms to a target surface. Therefore, in this section, we extend the framework to the inverse design of a conformable ribbon, where conformable implies that the ribbon's normal direction aligns with the normal vector of the target curved surface. Note that although we consider the clamped-clamped BCs here, this inverse design case can also be achieve with clamped-free BCs by solving Eq. (16) with an initial value condition $\mathbf{F}(0) = 0$ and $\mathbf{M}(0) = 0$. To achieve this, we first establish the geometric foundation for conformable ribbons on curved surfaces.

In our analysis, the conformable ribbon is modeled as a ruled surface:

$$\boldsymbol{r}(s,u) = \boldsymbol{\Gamma}(s) + u\boldsymbol{v}. \tag{24}$$

Here, $s$ denotes the arc-length parameter along the ribbon's centre line, and $u$ is a transverse parameter associated with the ribbon's width. The vector $\boldsymbol{v} = a\mathbf{d}_3 + b\mathbf{d}_1$, with $\sqrt{a^2+b^2} = 1$, is a unit vector lying in the $\{\mathbf{d}_3, \mathbf{d}_1\}$ plane, where $\mathbf{d}_3$ is the tangent vector and $\mathbf{d}_1$ is the material director along the transverse direction of the ribbon as shown in Fig. 8(A). For a conformable ribbon, the surface normal of the ribbon coincides with the normal vector of the target curved surface. As a result, the material frame of the ribbon is aligned with the Darboux frame of the surface (Do Carmo, 2016; Abbena et al., 2017). The material frame of the ribbon can be written as:

$$\begin{pmatrix} \mathbf{d}_3' \\ \mathbf{d}_1' \\ \mathbf{d}_2' \end{pmatrix} = \begin{pmatrix} 0 & \kappa_g & \kappa_n \\ -\kappa_g & 0 & \tau_g \\ -\kappa_n & -\tau_g & 0 \end{pmatrix} \begin{pmatrix} \mathbf{d}_3 \\ \mathbf{d}_1 \\ \mathbf{d}_2 \end{pmatrix}, \tag{25}$$

where $\kappa_n$ is the normal curvature, $\kappa_g$ is the geodesic curvature and $\tau_g$ is the geodesic torsion. For a conformable ribbon, since its normal direction is aligned with that of the target curved surface, the tangent plane of the ribbon must coincide with the tangent plane of the surface at every point. Consequently, the $\mathbf{d}_2$ component of the partial derivative $\partial_s \boldsymbol{r}(s,u)$ must vanish, i.e., $\mathbf{d}_2 \cdot \partial_s \boldsymbol{r}(s,u) = 0$, where $\mathbf{d}_2$ denotes the surface normal direction in the Darboux frame.

$$\boldsymbol{r}'(s,u) = u\big(a\kappa_n + b\tau_g\big)\mathbf{d}_2 + \big(1 - ub\kappa_g\big)\mathbf{d}_3 + ua\kappa_g\mathbf{d}_1. \tag{26}$$

Thus, we have $a\kappa_n + b\tau_g = 0$, and finally the equation of the ribbon can be derived as:

$$\boldsymbol{r}(s,u) = \boldsymbol{r}(s) + \frac{u}{\sqrt{\kappa_n^2 + \tau_g^2}}(\tau_g\mathbf{d}_3 - \kappa_n\mathbf{d}_1). \tag{27}$$

Using Eq. (27), we can derive conformable ribbon with the given target surface and the helix space curve.

The hemispherical helix is a critical morphology for antenna systems due to its ability to approach the Chu-Harrington limit (Chu, 1948; Kong et al., 2016), making it highly valuable in radio frequency applications. Its unique geometry enhances radiation efficiency while maintaining a small form factor, which is essential for modern miniaturized radar designs. As shown in Fig. 8(B), for the traditional hemispherical helix antennas the supporter is necessary to overcome the effect of gravity, but we can achieve the inverse design of deployable and conformable hemisphere helix ribbon with only two clamped ends by inverse elastica theory. Here, we consider the inverse design of a conformable hemispherical helix (Eq. (28)).

$$\begin{cases} x(t) = R\sin(\pi(2-t)/4)\cos(5\pi(2-t)) \\ y(t) = R\sin(\pi(2-t)/4)\sin(5\pi(2-t)) \\ z(t) = R\cos(\pi(2-t)/4) \end{cases} \qquad t \in [0.1, 1.9]. \tag{28}$$

For ease of transportation, our objective is to design a conformable hemispherical helical ribbon with minimal height variance, as illustrated in Fig. 8(C). Two key dimensionless physical parameters are considered in the design: the gravity-elasticity number, defined as $\gamma = \frac{\rho g L^3}{E w^2}$, and the width-to-thickness ratio, $\alpha = \frac{w}{t}$, where $w$ and $t$ denote the ribbon's width and thickness, respectively, $\rho$ is the material density, $g$ is the gravitational acceleration, $L$ is the arc length of the ribbon, and $E$ is the Young's modulus. Note that gravity is applied by setting the external force load $\bar{\mathbf{f}} = -\rho A g\{q_1q_3 - q_0q_2,\ q_2q_3 + q_0q_1,\ q_0^2 + q_3^2 - 1/2\}$ in Eq. (16). To achieve the desired geometry, we control the $z$-coordinate of the left end of the helix, $z(1.9)$, through an optimization procedure. The loss function is formulated as:

$$f = (z(1.9) - z_{tmp})^2. \tag{29}$$

We gradually change $z_{tmp}$ from $R$ to $-R$, and shows height variance $\lambda$ in Fig. 8(D) for $\alpha = 10$. It shows that if there is no gravity, the minimal volume point is in $z_{tmp} = 0$ and gravity causes the minimum point to shift to the right. As the gravity-elasticity number $\gamma$ gradually increases, the minimum value of the curve first decreases and then increases, which means that we can obtain the optimal value of $\lambda$ by adjusting the $w$ of the ribbon, thereby minimizing the volume of the antenna. For different width-to-thickness ratio $\alpha$, we plot the minimal $\lambda$ as a function of $\gamma$ in Fig. 8(E), which can provide guidance for the engineering design of hemispherical helix antennas. We selected a copper antenna as an specific example, which means the density $\rho = 8.96\ kg/m^3$, Young's modulus $E = 120\ GPa$. Suppose the radius $R$ is 0.05 $m$ and the length of the ribbon is 0.922 $m$, the width-thickness ratio $\alpha$ is 10 and we can read the optimal $\gamma = 0.078$ as shown in Fig. 8(E) As a result, the fabrication width of the ribbon can be finally estimated $w = \sqrt{\rho g L^3/E\gamma} \approx 2.7\ mm$.

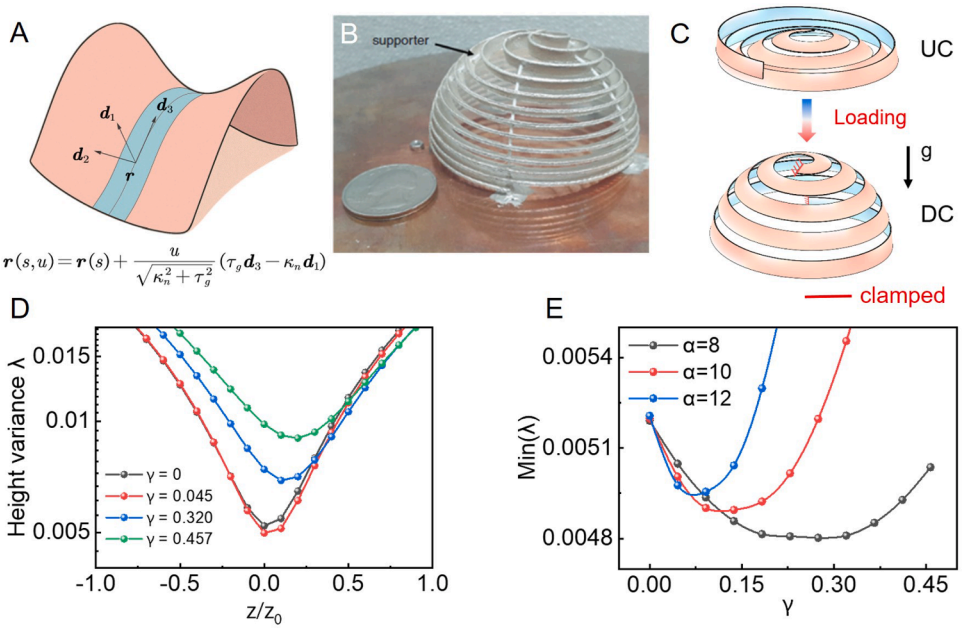


**Fig. 8.** The optimal inverse design of a deployable and conformable hemispherical helix antenna. (A) The illustration of a deployable and conformable ribbon. (B) The small hemispherical helix antennas with supporter (Kong et al., 2016). (C) Morphing of conformable hemispherical helix ribbon by clamped-clamped BCs with gravity effect considered. (D) The height variance with different elastic-gravity parameter as a function of normalized height $z/R$. (E) The minimal value of height variance $\lambda$ for different width-thickness ratio $\alpha$ as a function of elastic-gravity parameter $\gamma$.

## 4. Discussion

Building upon the theoretical framework presented in Section 2, this study has established the inverse elastica theory as a direct solution method for determining UC from DC. The proposed methodology has demonstrated remarkable versatility through several examples: the inverse design of a trefoil knot and the discretization of helical curved surfaces with variable Gaussian curvatures. The key contributions of this work can be systematically summarized as follows: Firstly, we have formulated the inverse elastica theory as a novel approach for the inverse design of elastic rods. Comparative analysis reveals that the governing equations of inverse elastica exhibit significantly reduced nonlinearity compared to the forward solving of Kirchhoff rod model. Then our investigation elucidates the fundamental origin of multiple solutions in the inverse problem. These non-unique solutions arise from the inherent flexibility in specifying force and moment BCs, which can be arbitrarily supplied through displacement constraints. Moreover, by reformulating the inverse elastica equations as a BVP, we introduce the fundamental concept of inverse loading. This novel approach enables direct determination of UC from prescribed DC through controlled boundary displacements, thereby establishing a rigorous mathematical duality with the classical elastica theory. To address cases where desired UC characteristics cannot be conveniently expressed as BVP in Eq. (16), we further develop a theory-assisted optimization strategy within our theoretical framework.

Although the theoretical framework of inverse elastica has been established, several open questions remain for future investigation. First, we are developing an inverse discrete elastic rod (InvDER) simulator capable of determining the UC from a given DC under prescribed inverse loading based on inverse elastica (Li et al., 2025a). This computational tool will serve as the inverse counterpart to the widely used DER simulator, which has found extensive applications in mechanics, computer graphics, biophysics, and related fields. For form-finding tasks involving more complex structures such as gridshells, which are often intractable by analytical means (Baek et al., 2018; Qin et al., 2020), the InvDER framework holds great promise for enabling direct numerical solutions. Second, similar to forward problems, the inverse loading framework exhibits bifurcation phenomena when analyzed using numerical continuation methods (Yu and Hanna, 2019; Yu et al., 2021). A comprehensive understanding of the physical significance of these bifurcations in the context of inverse problems has yet to be developed. Third, inspired by Kirchhoff's classical analogy between elastic rod theory and rigid body dynamics (Kehrbaum and Maddocks, 1997), we plan to explore potential mathematical analogies for the inverse elastica formulation. Such analogies may offer deeper theoretical insights and unify inverse deformation mechanics with other areas of applied physics and geometry. From an engineering perspective, we propose to relax the strict target shape constraints of conformable hemispherical helical ribbons in order to improve spatial efficiency. For instance, by optimizing the pitch distribution of the helix as DC, it may be possible to achieve reduced height variance and more compact deployable structures. Lastly, experimental fabrication of morphing hemispherical helical antennas designed via the inverse elastica theory is a crucial direction for future work.

## 5. Conclusion

We present inverse elastica as a general framework, based on the classical Kirchhoff rod model, for determining the UC from a prescribed DC of morphing slender structures by reformulating the inverse problem as a boundary-value problem. Building on inverse elastica, we propose a theory-assisted optimization method for inverse design of complex spatial curves. Compared with the forward optimization method, it has higher efficiency. With this theory-assisted optimization method, we further achieved the inverse design of complex spatial configurations such as trefoil knots and helix discretized curved surfaces with varying Gaussian curvatures, validated with both DER simulations and experiments. Looking ahead, future work includes the development of an inverse discrete elastic rod (Inverse DER) solver, the analysis of bifurcation behavior, and the fabrication of deployable and conformable hemisphere helix antennas. These directions will be essential for extending the applicability of the framework to fields such as flexible electronics, aerospace systems, and reconfigurable structures. In conclusion, inverse elastica theory provides a robust and theoretical foundation for the inverse design of morphing slender structures, with broad potential for applications in radio-frequency systems, deployable architecture, soft robotics and other related fields.

## CRediT authorship contribution statement

**JiaHao Li:** Conceptualization, Writing - original draft, Methodology, Software, Investigation, Data curation, Validation; **Weicheng Huang:** Writing – original draft, Methodology, Supervision, Formal analysis, Validation, Software; **YinBo Zhu:** Writing – review & editing, Resources, Funding acquisition; **Luxia Yu:** Writing – review & editing, Formal analysis; **Xiaohao Sun:** Writing – review & editing, Formal analysis, Validation; **Mingchao Liu:** Conceptualization, Writing – review & editing, Methodology, Supervision, Formal analysis, Validation; **HengAn Wu:** Conceptualization, Writing – review & editing, Validation, Supervision, Resources, Project administration, Funding acquisition.

## Data availability

Data will be made available on request.

## Declaration of competing interest

The authors declare that they have no known competing financial interests or personal relationships that could have appeared to influence the work reported in this paper.

## Acknowledgements

We are grateful to Haiyi Liang, Linghui He and Liu Wang at the University of Science and Technology of China for their insightful discussions. The research leading to these results has received funding from the National Natural Science Foundation of China (12388101, 12232016, 52575322), the USTC Tang Scholar and the Fundamental Research Funds for the Central Universities (WK2090000087), and from the University of Birmingham via the start-up funding (M.L.). The numerical calculations were performed on the supercomputing system in Hefei Advanced Computing Center and the Supercomputing Center of University of Science and Technology of China.

## Appendix A. 2D case: Inverse design of an arc

The inverse elastica has analytical solution for 2D cases. We consider the inverse design of planar curve as follows.

For the 2D case, we first expand $\mathbf{F}$ and $\mathbf{f}$ in local frame: $\{\mathbf{d}_3, \mathbf{d}_1\}$; $\mathbf{M}$ and $\mathbf{m}$ in local frame $\mathbf{d}_2$ and then use the motion equation of frame: $(\mathbf{d}_3)' = \omega_2 \mathbf{d}_1$, $(\mathbf{d}_1)' = -\omega_2 \mathbf{d}_3$, where $\omega_2$ is the material curvature of DC, to simplify Eqs. (1) ~ (2). It reads

$$\begin{cases} (F_1)' = -F_3\omega_2 + f_1 \\ (F_3)' = F_1\omega_2 + f_3 \\ (M_2)' = -F_1 + m_2 \end{cases}, \tag{A.1}$$

where $F_i$ and $f_i$ is component of $\mathbf{F}$ and $\mathbf{f}$ on $\mathbf{d}_i (i = 1, 3)$, $M_2$ and $m_2$ are components of $\mathbf{M}$ and $\mathbf{m}$ on $\mathbf{d}_2$. For the kirchhoff rod model with linear elastic material, the bending constitutive can be written as:

$$M_2 = EI_2(\omega_2 - \omega_{20}). \tag{A.2}$$

The geometry of elastica meets the following relationship

$$(\theta)' = \omega_2, \tag{A.3}$$

where $\theta$ is the rotation angle of DC. For the elastica without external load and moment $\bar{\mathbf{f}}$ and $\bar{\mathbf{m}}$, Eq. (A.1) ~ (A.3) can be simplified to the classic form derived by Lagrange in 1771 (Matsutani, 2024),

$$(EI_2((\theta)' - \omega_{20}))' - F_x \sin\theta + F_y \cos\theta = 0, \tag{A.4}$$

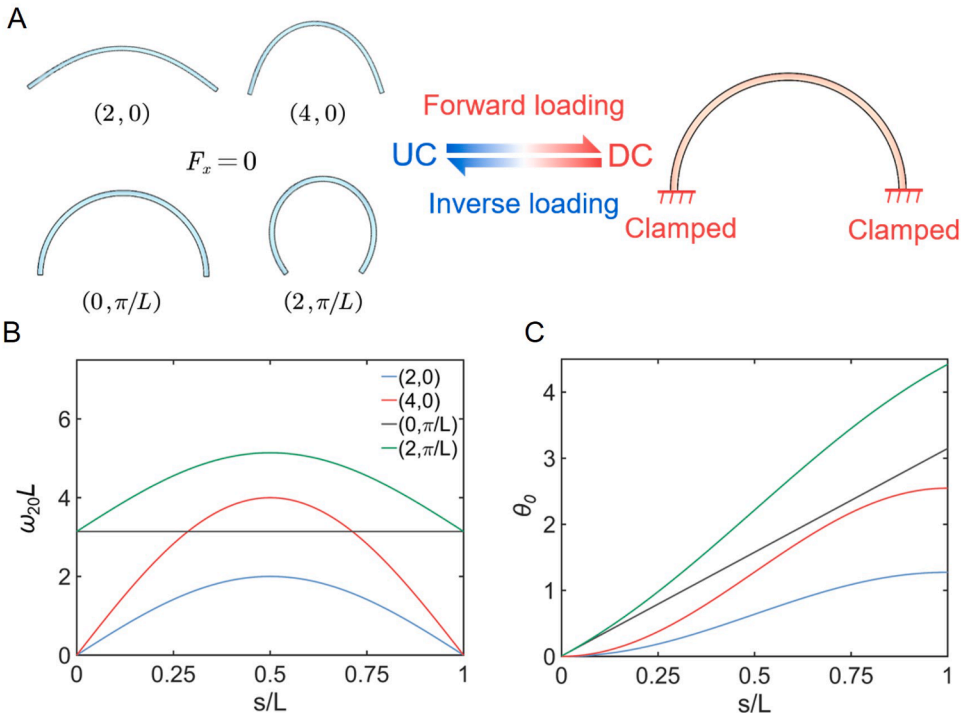


**Fig. A.9.** The inverse design of an arc. A family of UC deform into a target arc-shaped DC with displacement boundary condition applied. (A) UC deforming into the arc-shaped DC for differential parameters $(F_y/(\omega_2 EI_2), \omega_0)$. (B) Dimensionless material curvature as a function of normalized arc length $s/L$. (C) Rotation angle $\theta$ as a function of normalized arc length $s/L$.

where $F_x$ and $F_y$ are the horizontal and vertical components of the internal force and $F_1$ can be converted from them: $F_1 = F_y \cos\theta - F_x \sin\theta$. For the inverse problem, $\theta$, which describes the DC is a known variable, and we need to solve $\omega_{20}$ instead of $\theta$. Under this situation, the nonlinearity of Eq. (A.4) is reduced, which is consistent with the reduced nonlinearity in Section 2.3. As a result, $\omega_{20}$ can be directly obtained by integrating Eq. (A.4), i.e.,

$$\omega_{20} = \int_0^s \left(\theta_{ss} + \frac{F_y \cos\theta - F_x \sin\theta}{EI_2}\right) ds + \omega_0. \tag{A.5}$$

Eq. (A.5) raises a natural question: how should the parameters $F_y$, $F_x$, and $\omega_0$ be chosen? To gain insight, we consider a toy model in which the DC is an arc, specified by $\theta = \omega_2 s$ and $\omega_2$ is constant. Substituting this expression into Eq. (A.5) yields an analytical expression for the corresponding material curvature of UC $\omega_{20}$,

$$\omega_{20} = \frac{F_x \cos(\omega_2 s) + F_y \sin(\omega_2 s)}{\omega_2 EI_2} + \omega_0. \tag{A.6}$$

Eq. (A.6) provides an analytical relation for the material curvature $\omega_{20}$ of a given DC, governed by the external forces $F_x$, $F_y$, the bending stiffness $EI_2$, and an integration constant $\omega_0$.

To build physical intuition, consider a clamped-clamped beam subjected to pure bending ($F_x = F_y = 0$). In this case, Eq. (A.6) reduces to $\omega_{20} = \omega_0 = \text{const}$. When $\omega_0 = 0$, UC is a straight beam; when $\omega_0 = \omega_2$, UC corresponds to identical curvatures without end loads. For nonzero terminal loads ($F_x, F_y \neq 0$), Eq. (A.6) yields nontrivial inverse elastica solutions beyond the intuitive arc or straight-line configurations, as shown in Fig. A.9(A). The resulting UCs are parameterized by $(F_y/(\omega_2 EI_2), \omega_0)$, with the corresponding normalized curvature $\omega_{20}L$ and rotation angle $\theta_0$ illustrated in Figs. A.9(B)–(C).

## Appendix B. 3D case: Inverse design of a helix

We consider the DC as a helix with constant $\boldsymbol{\omega}$ and $\boldsymbol{\Omega}$. The component form of Eq. (16) reads

$$\begin{cases} (F_1)' = F_2\omega_3 - F_3\omega_2 + f_1 \\ (F_2)' = F_3\omega_1 - F_1\omega_3 + f_2 \\ (F_3)' = F_1\omega_2 - F_2\omega_1 + f_3 \\ EI_1(\omega_1 - \omega_{10})' = EI_2(\omega_2 - \omega_{20})\omega_3 - GJ(\omega_3 - \omega_{30})\omega_2 + F_2 + m_1 \\ EI_2(\omega_2 - \omega_{20})' = GJ(\omega_3 - \omega_{30})\omega_1 - EI_1(\omega_1 - \omega_{10})\omega_3 - F_1 + m_2 \\ GJ(\omega_3 - \omega_{30})' = EI_1(\omega_1 - \omega_{10})\omega_2 - EI_2(\omega_2 - \omega_{20})\omega_1 + m_3 \\ (q_{00})' = -1/2(q_{01}\omega_{10} + q_{02}\omega_{20} + q_{03}\omega_{30}) \\ (q_{01})' = 1/2(q_{00}\omega_{10} - q_{03}\omega_{20} + q_{02}\omega_{30}) \\ (q_{02})' = 1/2(q_{03}\omega_{10} + q_{00}\omega_{20} - q_{01}\omega_{30}) \\ (q_{03})' = 1/2(q_{01}\omega_{20} - q_{02}\omega_{10} + q_{00}\omega_{30}) \\ (x_0)' = 2(q_{01}q_{03} + q_{00}q_{02}) \\ (y_0)' = 2(q_{02}q_{03} - q_{00}q_{01}) \\ (z_0)' = 2(q_{03}^2 + q_{00}^2 - 1/2) \end{cases}. \tag{B.1}$$

Neglecting external loads ($f_i = m_i = 0, i = 1, 2, 3$), Eq. (B.1) can be solved under prescribed end displacements, analogous to the displacement-controlled Kirchhoff formulation. We compare forward and inverse loading via numerical continuation, a standard technique in Kirchhoff rod analysis (Doedel et al., 2007; Yu and Hanna, 2019; Yu et al., 2021, 2023; Shi et al., 2025).

Starting from a helix spring with circular cross section,

$$\begin{cases} x(t) = 0.5\cos(6\pi t), \\ y(t) = 0.5\sin(6\pi t), \qquad t \in [0.1, 1.1], \\ z(t) = t, \end{cases} \tag{B.2}$$

we extend its end-to-end distance from 1.1 m to 6.1 m as shown in Fig. B.10(A)). During forward loading, the spring experiences smaller deformation at its two ends. This concentrates the stretching in the middle part, resulting in a decreased radius at mid-span. In contrast, during inverse loading, larger deformation occurs at the ends, which leads to a correspondingly larger mid-span radius, as seen in the blue spring. Correspondingly, Figs. B.10(B)-(C) show that forward loading causes gradual curvature and torsion changes, whereas inverse loading produces sharper variations. The difference stems from the distinct formulations of elastica and inverse-elastica theories. DER simulations further confirm that compressing the UC from inverse loading reproduces the original DC curvature and torsion (green markers in Figs. B.10(B)-(C)).

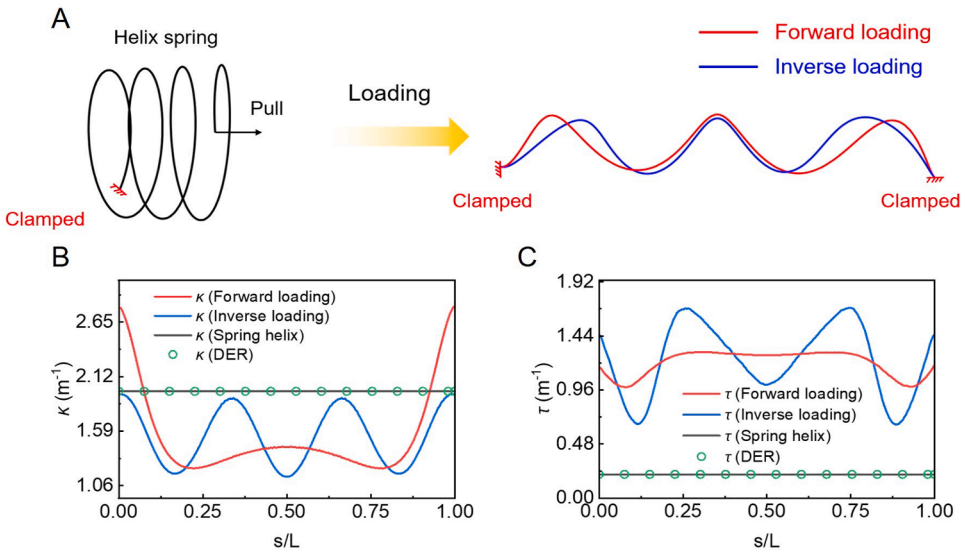


**Fig. B.10.** Comparison between inverse and forward loading. (A) Deformation of a helical spring under inverse and forward loading. (B) Curvature and (C) torsion distributions. Green dots denote DER validation results.

## Appendix C. The comparison between forward-optimization and the theory-assisted optimization.

In this section, we compare the forward optimization method and the theory-assisted optimization method in this work. Note that the procedure of the theory-assisted optimization has been explained in Section 3, now we define the forward optimization as follows for the inverse design of planar curve. Suppose we discretize a planar curve into $n+2$ vertices. First, we generate a series of rotation angle $\theta_i^k$, where $i = 1, 2, 3 \ldots, n$ and $k = 1$ represents the first iteration. Then, we generate a planar curve $\{x_i^k, y_i^k\}$ with $\theta_i^k$. And use the forward solver to solve the rotation angle $\theta_{i,for}^k$ of the DC. It is important to note that the variation of $\theta_i^k$ across iterations $k$ leads to different UCs, causing the forward solver to potentially yield $\theta_{i,\mathrm{for}}^k$ on different solution branches. Consequently, careful selection of the loading path is required. Later, we define the loss function forward fval as $fval = \sum_{i=1}^{n} \left(\theta_{i,for}^k - \theta_{i,target}^k\right)^2$. Finally, we optimize $f$ under the constrains $\mathrm{C}(x_i^k, y_i^k, \theta_i^k) = 0$. This procedure is also suitable for the inverse design of 3D curve, the only difference is that the rotation angle should be changed to the Euler angle for spatial rotation.

To compare the two types of optimization method, we consider the inverse design problem of a cardioid as defined by Eq. (C.1). The problem is defined as follows: for the clamped-clamped BCs, find the UC of the cardioid, which meets the distance of the two ends of UC is $0.1L$, $L$ is the length of the cardioid. Thus for the forward optimization, we use DER as the forward solver and define the constrains as Eq. (C.2). For theory-assisted optimization the loss function is defined as $(\sqrt{(x(1)-x(0))^2+(y(1)-y(0))^2}-0.1)^2$ according to Section 3. The comparison of results between forward optimization and the theory-assisted optimization are shown in Fig. C.11.

$$\begin{cases} x = \dfrac{1}{8}(1-\cos\theta)\cos\theta \\ y = \dfrac{1}{8}(1-\cos\theta)\sin\theta \end{cases} \qquad 0 \le \theta \le 2\pi \tag{C.1}$$

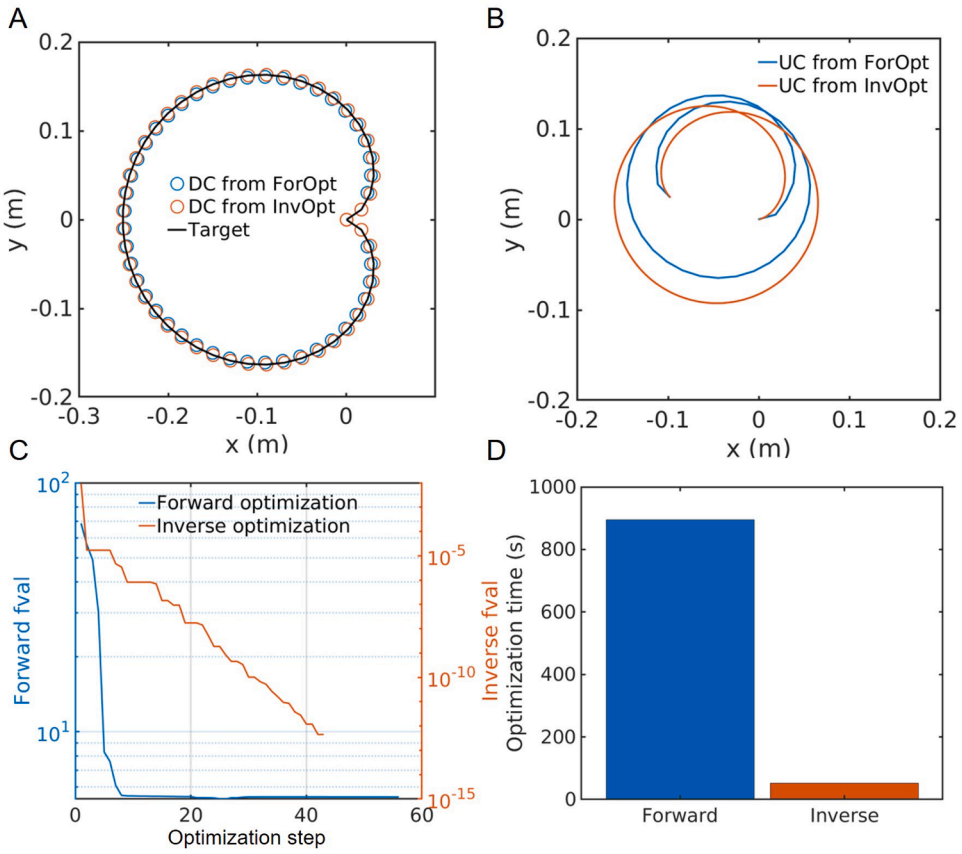


**Fig. C.11.** The comparison between forward optimization and the theory-assisted optimization. (A) The DCs obtained from the forward loading of the UCs and the target cardioid. (B) The UCs for these two methods respectively. The UC from forward optimization is recovered from the optimized discrete rotation angle $\theta_i (i = 1, 2, \ldots, n)$. We use 52 vertices for this forward-optimization case, which means $n = 50$. (C) Loss function values for forward and inverse optimizations. (D) The time consumption for forward and inverse optimizations.

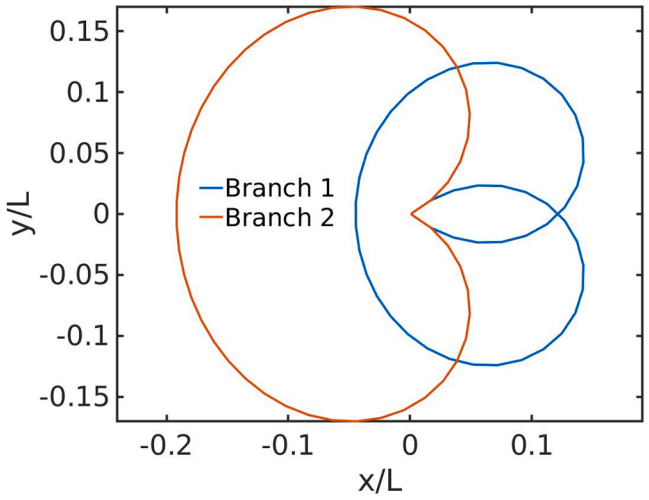


**Fig. C.12.** Two branches of DCs from guessed UCs under clamped-clamped BCs.

$$C(x_i^k, y_i^k, \theta_i^k) = \sqrt{(x_1^k - x_n^k)^2 + (y_1^k - y_n^k)^2} - 0.1 = 0 \tag{C.2}$$

**Time consumption** The theory-assisted optimization method requires significantly less time than the forward optimization, as shown in Fig. C.11D. There are two main reasons for this. First, forward optimization involves $n$ optimization variables, whereas the theory-assisted method only requires three for 2D case, resulting in substantially reduced time consumption. Second, each iteration of forward optimization necessitates running the forward solver to obtain the DC, which also incurs considerable time costs.

**Local minima** Additionally, since slender structures often exhibit bifurcation behavior under forward loading (Yu and Hanna, 2019; Yu et al., 2021), there is a high likelihood of entering undesired branches during forward solving. Therefore, the loading path for forward solver must be chosen carefully, as forward optimization is prone to being trapped in local minima. As shown in Fig. C.12, both planar curves are results obtained from the forward solver under clamped–clamped BCs; however, to minimize $\sum_{i=1}^{n}\left(\theta_{i,for}^k - \theta_{i,target}^k\right)^2$ branch 2 is required rather than branch 1. Therefore, we need to carefully adjust the loading path in each optimization step to avoid converging to branch 2 for this case. In contrast, the theory-assisted optimization method does not depend on the loading path, thus avoiding entrapment in local minima.

## Appendix D. The equations of helix discretized curved surfaces and experiment settings.

### The equations of helix discretized curved surfaces

The equation of helix discretized cone is:

$$\begin{cases} x = R(1 - t/2)\cos(2\pi N t) \\ y = R(1 - t/2)\sin(2\pi N t) \\ z = Rt \end{cases} \qquad t \in [0, 1.5], \tag{D.1}$$

where $R = 0.05, N = 2$.

The equation of helix discretized sphere is:

$$\begin{cases} x = R\cos(2\pi N t)\sin(\pi/2t) \\ y = R\sin(2\pi N t)\sin(\pi/2t) \\ z = R\cos(\pi/2t) \end{cases} \qquad t \in [0.1, 1.9], \tag{D.2}$$

where $R = 0.05, N = 5$.

The equation of helix discretized hyperboloid is:

$$\begin{cases} x = R\left((t-1)^2 + 0.5\right)\cos(\pi N t) \\ y = R\left((t-1)^2 + 0.5\right)\sin(\pi N t) \\ z = tR/2 \end{cases} \qquad t \in [0, 1.9], \tag{D.3}$$

where $R = 0.05, N = 5$.

### Experiment settings

The material properties employed in both the simulations and theoretical analysis are specified as follows: the Young's modulus is $2 \times 10^7$ Pa, and the radius of the circular cross-section is 0.0015 m (i.e., 1.5 mm).The STL models were built with OpenSCAD. The optimized helical structures, discretized into curved surface elements, were fabricated using a Bamboo X1C 3D printer with SLA resin. These slender SLA-printed structures are capable of sustaining small strains while exhibiting significant rotational deformation behavior. The effect of gravity is not considered in these three cases.

## Appendix E. The discrete elastic rod method.

**The loading steps of DER verifications**

To validate the proposed inverse elastica theory, simulations based on the Discrete Elastic Rod (DER) are conducted (Bergou et al., 2008; Huang et al., 2025; Jawed et al., 2018). The loading procedure consists of the following steps: first, the positions of two nodes at the left end of the UC are fixed. Next, the positions of two nodes at the right end of the UC are gradually displaced to match those of the corresponding nodes at the right end of DC. Finally, the material director at the terminal edge of the UC is rotated to align with that of the DC.

**Discrete elastic rod algorithm**

The discrete elastica rod (DER) method is used to validate our inverse elastica theory by forward loading from the UC to the DC (Bergou et al., 2008; Huang et al., 2025; Jawed et al., 2018). As shown in Fig. E.13(A), a slender structure is discretized into $N$ nodes $\boldsymbol{x}_0, \boldsymbol{x}_1, \ldots, \boldsymbol{x}_{N-1}$, forming $N-1$ edge vectors $\boldsymbol{e}^i = \boldsymbol{x}_{i+1} - \boldsymbol{x}_i$ for $i = 0, \ldots, N-2$. Subscripts denote node-based quantities and superscripts denote edge-based quantities. Each edge $\boldsymbol{e}^i$ has an orthonormal reference frame $\{\mathbf{d}_1^i, \mathbf{d}_2^i, \boldsymbol{t}^i\}$ and a material frame $\{\boldsymbol{m}_1^i, \boldsymbol{m}_2^i, \boldsymbol{t}^i\}$, sharing the tangent $\boldsymbol{t}^i = \boldsymbol{e}^i / \|\boldsymbol{e}^i\|$. The reference frame is updated via parallel transport, and the material frame is obtained by applying a twist angle $\theta^i$ (Fig. E.13(B)). The generalized coordinate vector is $\boldsymbol{q} = [\boldsymbol{x}_0, \theta^0, \boldsymbol{x}_1, \theta^1, \ldots, \boldsymbol{x}_{N-2}, \theta^{N-2}, \boldsymbol{x}_{N-1}]^T$, with $4N-1$ degrees of freedom (DOF), where $(\cdot)^T$ denotes vector transpose.

**Strain definitions:**

*Stretching strain:*

$$\varepsilon^i = \frac{\|\boldsymbol{e}^i\|}{\|\bar{\boldsymbol{e}}^i\|} - 1 \tag{E.1}$$

where $\|\cdot\|$ is the norm, and $\bar{\boldsymbol{e}}^i$ is the reference edge vector.

*Bending strain:* The Darboux binormal vector is

$$(\kappa \boldsymbol{b})_i = \frac{2\boldsymbol{e}^{i-1} \times \boldsymbol{e}^i}{\|\boldsymbol{e}^{i-1}\|\|\boldsymbol{e}^i\| + \boldsymbol{e}^{i-1} \cdot \boldsymbol{e}^i} \tag{E.2}$$

with magnitude $\|(\kappa \boldsymbol{b})_i\| = 2\tan(\phi_i/2)$.

Material curvatures can be calculated as bending strain:

$$\kappa_i^{(1)} = \frac{1}{2}(\boldsymbol{m}_2^{i-1} + \boldsymbol{m}_2^i) \cdot (\kappa \boldsymbol{b})_i \tag{E.3}$$

$$\kappa_i^{(2)} = -\frac{1}{2}(\boldsymbol{m}_1^{i-1} + \boldsymbol{m}_1^i) \cdot (\kappa \boldsymbol{b})_i \tag{E.4}$$

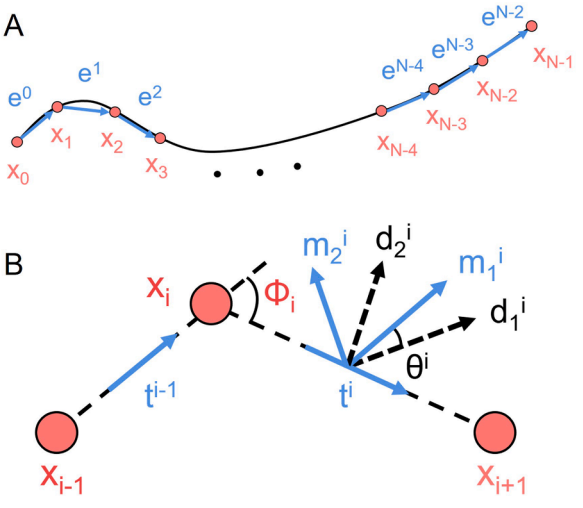


**Fig. E.13.** The schematic diagram of discrete elastic rod algorithm. (A) The slender structure as a discrete cosserate curve. (B) The bending element and the associated material frame and reference frame.

*Twisting strain:*

$$\tau_i = \theta^i - \theta^{i-1} + m_i \tag{E.5}$$

where $m_i$ is the reference twist. Eq. (E.5) expresses the total twist as the sum of reference twist and relative twist.

**Elastic energies:**

*Stretching energy:*

$$E_s = \frac{1}{2}\sum_{i=0}^{N-2} EA(\varepsilon^i)^2 \|\bar{\boldsymbol{e}}^i\| \tag{E.6}$$

*Bending energy:*

$$E_b = \frac{1}{2}\sum_{i=1}^{N-2} \frac{1}{\Delta l_i}\left[EI_1(\kappa_i^{(1)} - \bar{\kappa}_i^{(1)})^2 + EI_2(\kappa_i^{(2)} - \bar{\kappa}_i^{(2)})^2\right] \tag{E.7}$$

*Twisting energy:*

$$E_t = \frac{1}{2}\sum_{i=1}^{N-2} \frac{GJ}{\Delta l_i}(\tau_i)^2 \tag{E.8}$$

where $\Delta l_i$ is the Voronoi length at node $\boldsymbol{x}_i$.

**Time integration (Implicit Euler):**

Let $\boldsymbol{v} = \dot{\boldsymbol{q}}$. The update from $t_k$ to $t_{k+1} = t_k + h$ follows:

$$\mathbb{M}(\boldsymbol{q}_{k+1} - \boldsymbol{q}_k - h\boldsymbol{v}_k) - h^2(\boldsymbol{F}^{\text{int}}_{k+1} + \boldsymbol{F}^{\text{ext}}_{k+1}) = \boldsymbol{0} \tag{E.9}$$

where $\boldsymbol{F}^{\text{int}}_{k+1} = -\frac{\partial}{\partial \boldsymbol{q}_{k+1}}(E_s + E_b + E_t)$, and $\boldsymbol{F}^{\text{ext}}_{k+1}$ is the external force (e.g., gravity). $\mathbb{M}$ is the lumped mass matrix.

The Jacobian matrix for Eq. (E.9) is

$$\mathbb{J}_{ij} = \mathbb{M}_{ij} - h^2\left(-\frac{\partial^2(E_s + E_b + E_t)}{\partial q_i \partial q_j}\right) \tag{E.10}$$

where $q_i$ is the $i$-th component of $\boldsymbol{q}$. The Jacobian $\mathbb{J}$ is banded, and the time complexity is $\mathcal{O}(N)$.

## Appendix F. Vedio of DER verification

The forward verification for the elastic deformation of trefoil knot, helix discretized torus, cone, sphere and hyperboloid surfaces from UC to DC.

## References


Abbena, E., Salamon, S., Gray, A., 2017. Modern differential geometry of curves and surfaces with Mathematica. Chapman and Hall/CRC.

Aharoni, H., Xia, Y., Zhang, X., Kamien, R.D., Yang, S., 2018. Universal inverse design of surfaces with thin nematic elastomer sheets. Proceedings of the National Academy of Sciences 115 (28), 7206–7211.

Armon, S., Efrati, E., Kupferman, R., Sharon, E., 2011. Geometry and mechanics in the opening of chiral seed pods. Science 333 (6050), 1726–1730.

Audoly, B., Pomeau, Y., 2000. Elasticity and geometry. In: Peyresq Lectures on Nonlinear Phenomena. World Scientific, pp. 1–35.

Baek, C., Sageman-Furnas, A.O., Jawed, M.K., Reis, P.M., 2018. Form finding in elastic gridshells. Proceedings of the National Academy of Sciences 115 (1), 75–80.

Benvenuto, R., Salvi, S., Lavagna, M., 2015. Dynamics analysis and GNC design of flexible systems for space debris active removal. Acta Astronaut. 110, 247–265.

Bergou, M., Wardetzky, M., Robinson, S., Audoly, B., Grinspun, E., 2008. Discrete elastic rods. In: ACM SIGGRAPH 2008 Papers, pp. 1–12.

Bertails-Descoubes, F., Derouet-Jourdan, A., Romero, V., Lazarus, A., 2018. Inverse design of an isotropic suspended kirchhoff rod: theoretical and numerical results on the uniqueness of the natural shape. Proceedings of the Royal Society A: Mathematical, Physical and Engineering Sciences 474 (2212), 20170837.

Boley, J.W., Van Rees, W.M., Lissandrello, C., Horenstein, M.N., Truby, R.L., Kotikian, A., Lewis, J.A., Mahadevan, L., 2019. Shape-shifting structured lattices via multimaterial 4d printing. Proceedings of the National Academy of Sciences 116 (42), 20856–20862.

Chen, Z., Majidi, C., Srolovitz, D.J., Haataja, M., 2011. Tunable helical ribbons. Appl. Phys. Lett. 98 (1).

Cheng, X., Fan, Z., Yao, S., Jin, T., Lv, Z., Lan, Y., Bo, R., Chen, Y., Zhang, F., Shen, Z., et al., 2023. Programming 3d curved mesosurfaces using microlattice designs. Science 379 (6638), 1225–1232.

Chu, L.J., 1948. Physical limitations of omni-directional antennas. J. Appl. Phys. 19 (12), 1163–1175.

Derouet-Jourdan, A., Bertails-Descoubes, F., Daviet, G., Thollot, J., 2013. Inverse dynamic hair modeling with frictional contact. ACM Trans. Graph. (TOG) 32 (6), 1–10.

Derouet-Jourdan, A., Bertails-Descoubes, F., Thollot, J., 2010. Stable inverse dynamic curves. ACM Trans. Graph. (TOG) 29 (6), 1–10.

Do Carmo, M.P., 2016. Differential geometry of curves and surfaces: revised and updated second edition. Courier Dover Publications.

Doedel, E.J., Champneys, A.R., Dercole, F., Fairgrieve, T.F., Kuznetsov, Y.A., Oldeman, B., Paffenroth, R.C., Sandstede, B., Wang, X.J., Zhang, C.H., 2007. Auto-07p: continuation and bifurcation software for ordinary differential equations .

Efrati, E., Sharon, E., Kupferman, R., 2009. Elastic theory of unconstrained non-euclidean plates. J. Mech. Phys. Solids 57 (4), 762–775.

Fan, Z., Yang, Y., Zhang, F., Xu, Z., Zhao, H., Wang, T., Song, H., Huang, Y., Rogers, J.A., Zhang, Y., 2020. Inverse design strategies for 3d surfaces formed by mechanically guided assembly. Adv. Mater. 32 (14), 1908424.

Huang, W., Hao, Z., Li, J., Tong, D., Guo, K., Zhang, Y., Gao, H., Hsia, K.J., Liu, M., 2025. A tutorial on simulating nonlinear behaviors of flexible structures with the discrete differential geometry (DDG) method. Appl. Mech. Rev. 1–88.

Huang, W., Zou, H., Liu, H., Yang, W., Gao, J., Liu, Z., 2023. Contact dynamic analysis of tether-net system for space debris capture using incremental potential formulation. Adv. Space Res. 72 (6), 2039–2050.

Jawed, M.K., Novelia, A., O'Reilly, O.M., 2018. A primer on the kinematics of discrete elastic rods. Springer.

Kansara, H., Liu, M., He, Y., Tan, W., 2023. Inverse design and additive manufacturing of shape-morphing structures based on functionally graded composites. J. Mech. Phys. Solids 180, 105382.

Kehrbaum, S., Maddocks, J.H., 1997. Elastic rods, rigid bodies, quaternions and the last quadrature. Philos. Trans. R. Soc. Lond. Ser. A 355 (1732), 2117–2136.
Kim, Y., Parada, G.A., Liu, S., Zhao, X., 2019. Ferromagnetic soft continuum robots. Sci. Rob. 4 (33), eaax7329.
Kong, M., Shin, G., Lee, S.-H., Yoon, I.-J., 2016. Electrically small folded spherical helix antennas using copper strips and 3d printing technology. Electron. Lett. 52 (12), 994–996.
Lee, Y.-K., Xi, Z., Lee, Y.-J., Kim, Y.-H., Hao, Y., Choi, H., Lee, M.-G., Joo, Y.-C., Kim, C., Lien, J.-M., et al., 2020. Computational wrapping: a universal method to wrap 3d-curved surfaces with nonstretchable materials for conformal devices. Sci. Adv. 6 (15), eaax6212.
Li, J., Liu, M., Liang, H., Wu, H., Huang, W., 2025a. Inverse discrete elastic rod. arXiv preprint arXiv:2512.06830.
Li, J., Sun, X., He, Z., Hou, Y., Wu, H., Zhu, Y., 2025b. Biomimetic turing machine: a multiscale theoretical framework for the inverse design of target space curves. J. Mech. Phys. Solids 196, 105999.
Li, J., Tong, D., Hao, Z., Zhu, Y., Wu, H., Liu, M., Huang, W., 2025c. Harnessing discrete differential geometry: a virtual playground for the bilayer soft robotics. Adv. Intell. Syst. , 2500141.
Ling, S., Tian, X., Zeng, Q., Qin, Z., Kurt, S.A., Tan, Y.J., Fuh, J. Y.H., Liu, Z., Dickey, M.D., Ho, J.S., et al., 2024. Tension-driven three-dimensional printing of free-standing field's metal structures. Nat. Electron. 7 (8), 671–683.
Liu, M., Domino, L., Vella, D., 2020. Tapered elasticæ as a route for axisymmetric morphing structures. Soft Matter 16 (33), 7739–7750.
Love, A. E.H., 1944. A treatise on the mathematical theory of elasticity. Courier Corporation.
Matsutani, S., 2024. Euler's original derivation of elastica equation. arXiv preprint arXiv:2411.09227.
Miller, J.T., Lazarus, A., Audoly, B., Reis, P.M., 2014. Shapes of a suspended curly hair. Phys. Rev. Lett. 112 (6), 068103.
Moulton, D.E., Grandgeorge, P., Neukirch, S., 2018. Stable elastic knots with no self-contact. J. Mech. Phys. Solids 116, 33–53.
O'Reilly, O.M., 2017. Modeling nonlinear problems in the mechanics of strings and rods. Springer.
Qin, L., Huang, W., Du, Y., Zheng, L., Jawed, M.K., 2020. Genetic algorithm-based inverse design of elastic gridshells. Struct. Multidiscip. Optim. 62, 2691–2707.
Qin, L., Zhu, J., Huang, W., 2022. A bottom-up optimization method for inverse design of two-dimensional clamped-free elastic rods. Int. J. Numer. Methods Eng. 123 (11), 2556–2572.
Rushen, 2019. Trimeresurus sabahi fucatus, banded pit viper - takua pa district, phang-nga province. https://commons.wikimedia.org/wiki/File:Trimeresurus_sabahi_fucatus,_Banded_pit_viper_-_Takua_Pa_District,_Phang-nga_Province_(46710893582).jpg. Image licensed under CC BY 2.0 via Wikimedia Commons.
Sawa, Y., Ye, F., Urayama, K., Takigawa, T., Gimenez-Pinto, V., Selinger, R. L.B., Selinger, J.V., 2011. Shape selection of twist-nematic-elastomer ribbons. Proceedings of the National Academy of Sciences 108 (16), 6364–6368.
Shen, Z., Hu, X., Tang, Z., Xiao, Y., Wang, S., Cheng, X., Zhang, Y., 2024. Curvature programming of freestanding 3d mesostructures and flexible electronics based on bilayer ribbon networks. J. Mech. Phys. Solids 191, 105766.
Shi, Q., Huang, W., Yu, T., Li, M., 2025. Double-eigenvalue bifurcation and multistability in serpentine strips with tunable buckling behaviors. J. Mech. Phys. Solids 195, 105922.
Shin, B., Ha, J., Lee, M., Park, K., Park, G.H., Choi, T.H., Cho, K.-J., Kim, H.-Y., 2018. Hygrobot: a self-locomotive ratcheted actuator powered by environmental humidity. Sci. Rob. 3 (14), eaar2629.
Siéfert, E., Reyssat, E., Bico, J., Roman, B., 2019. Bio-inspired pneumatic shape-morphing elastomers. Nat. Mater. 18 (1), 24–28.
Singer, S., Nelder, J., 2009. Nelder-mead algorithm. Scholarpedia 4 (7), 2928.
Sun, X., Wu, S., Dai, J., Leanza, S., Yue, L., Yu, L., Jin, Y., Qi, H.J., Zhao, R.R., 2022a. Phase diagram and mechanics of snap-folding of ring origami by twisting. Int. J. Solids Struct. 248, 111685.
Sun, X., Yue, L., Yu, L., Forte, C.T., Armstrong, C.D., Zhou, K., Demoly, F., Zhao, R.R., Qi, H.J., 2024. Machine learning-enabled forward prediction and inverse design of 4d-printed active plates. Nat. Commun. 15 (1), 5509.
Sun, X., Yue, L., Yu, L., Shao, H., Peng, X., Zhou, K., Demoly, F., Zhao, R., Qi, H.J., 2022b. Machine learning-evolutionary algorithm enabled design for 4d-printed active composite structures. Adv. Funct. Mater. 32 (10), 2109805.
Sydney Gladman, A., Matsumoto, E.A., Nuzzo, R.G., Mahadevan, L., Lewis, J.A., 2016. Biomimetic 4d printing. Nat. Mater. 15 (4), 413–418.
Timoshenko, S., 1925. Analysis of bi-metal thermostats. J. Opt. Soc. Am. 11 (3), 233–255.
Tong, D., Hao, Z., Li, J., Huang, W., 2025. Inverse design of planar clamped-free elastic rods from noisy data. Int. J. Numer. Methods Eng. 126 (5), e70018.
Van Rees, W.M., Vouga, E., Mahadevan, L., 2017. Growth patterns for shape-shifting elastic bilayers. Proceedings of the National Academy of Sciences 114 (44), 11597–11602.
Wang, T., Dai, Z., Potier-Ferry, M., Xu, F., 2023. Curvature-regulated multiphase patterns in tori. Phys. Rev. Lett. 130 (4), 048201.
Wang, T., Potier-Ferry, M., Xu, F., 2025. A nonlinear toroidal shell model for surface morphologies and morphogenesis. J. Mech. Phys. Solids 200, 106135.
Xu, S., Yan, Z., Jang, K.-I., Huang, W., Fu, H., Kim, J., Wei, Z., Flavin, M., McCracken, J., Wang, R., et al., 2015. Assembly of micro/nanomaterials into complex, three-dimensional architectures by compressive buckling. Science 347 (6218), 154–159.
Yang, X., Zhou, Y., Zhao, H., Huang, W., Wang, Y., Hsia, K.J., Liu, M., 2023. Morphing matter: from mechanical principles to robotic applications. Soft Sci. 3 (4), 38.
Yu, T., Dreier, L., Marmo, F., Gabriele, S., Parascho, S., Adriaenssens, S., 2021. Numerical modeling of static equilibria and bifurcations in bigons and bigon rings. J. Mech. Phys. Solids 152, 104459.
Yu, T., Hanna, J.A., 2019. Bifurcations of buckled, clamped anisotropic rods and thin bands under lateral end translations. J. Mech. Phys. Solids 122, 657–685.
Yu, T., Marmo, F., Cesarano, P., Adriaenssens, S., 2023. Continuous modeling of creased annuli with tunable bistable and looping behaviors. Proceedings of the National Academy of Sciences 120 (4), e2209048120.
Zhang, Y., Yang, J., Liu, M., Vella, D., 2022. Shape-morphing structures based on perforated kirigami. Extreme Mech. Lett. 56, 101857.